Q. 1067

UCRL-50007-76-2

HAZARDS CONTROL PROGRESS REPORT NO. 53

July through December 1976

February 15, 1977

Prepared for U.S. Energy Research & Development Administration under contract No. W-7405-Eng-48

LAWRENCE LIVERMORE LABORATORY

University of California/Livermore

Printed in the United States of America
Available from
National Technical Information Service
U.S. Department of Commerce
5285 Port Royal Road
Springfield, VA 22161
Price: Printed Copy $5.00 ; Microfiche $3.00

Page Range	Domestic Price	Page Range	Domestic Price
001–025	$ 3.50	326–350	10.00
026–050	4.00	351–375	10.50
051–075	4.50	376–400	10.75
076–100	5.00	401–425	11.00
101–125	5.50	426–450	11.75
126–150	6.00	451–475	12.00
151–175	6.75	476–500	12.50
176–200	7.50	501–525	12.75
201–225	7.75	526–550	13.00
226–250	8.00	551–575	13.50
251–275	9.00	576–600	13.75
276–300	9.25	601–up	*
301–325	9.75		

* Add $2.50 for each additional 100 page increment from 601 to 1,000 pages; add $4.50 for each additional 100 page increment over 1,000 pages.

Distribution Category
UC-41

LAWRENCE LIVERMORE LABORATORY
University of California/Livermore, California/94550

UCRL-50007-76-2

HAZARDS CONTROL PROGRESS REPORT NO. 53
July through December 1976

MS. date: February 15, 1977

Foreword

This report is divided into three major sections. The first section, Progress Reports, covers the status of activities undertaken or continuing during the period; additional reports or separate publications will cover the final results of these activities. The second section, Technical Notes, contains reports on interesting activities of a more limited scope on which further reporting is not anticipated. The third section lists recent publications.

Readers who are interested in more detail regarding any item may contact the authors of the reports who are listed in the Contents.

Contents

PROGRESS REPORTS

Radiation Protection
Continued Realistic Phantom Development (*R. V. Griffith, A. L. Anderson, C. A. Harder and P. N. Dean*) . . . 1
Calculated Response Matrix for a Collimated 2 X 2 NaI(Tl) Gamma-Ray Detector (*D. R. Slaughter*) . . . 3
Developments in a Combined Albedo Electrochemical Track Etch Personnel Neutron Dosimeter (*R. V. Griffith*) . . . 6
GAMRESP: A Computer Code to Calculate NaI(Tl) Gamma Detector Response Matrices (*R. E. Strout and D. W. Rueppel*) . . . 9
Industrial Hygiene
Performance Reliability of Self-Contained Breathing Apparatus Exposed (Stored) to Various Temperatures (*B. J. Held, C. P. Richards and R. D. Taylor*) . . . 12
SCBA Communications Study (*B. J. Held and C. P. Richards*) . . . 15
Instrument Development
Neutron Spectroscopy in the Energy Range 0.5-20 MeV Using a NE 213 Scintillator (*D. R. Slaughter, R. C. Kaifer, D. Fuess and D. W. Rueppel*) . . . 16
Transmission Anode X-Ray Tube Development (*J. L. Cate, Jr.*) . . . 18
Fire Safety
HFPA-Filter Smoke Plugging Tests Using the LLL Large Scale Fire Test Facility (*J. R. Gaskill, N. J. Alvares, D. G. Beason, H. W. Ford, Jr. and L. Davis*) . . . 23
Enhanced Filtration
Introduction (*G. O. Nelson, W. Bergman, H. H. Miller, R. D. Taylor, A. H. Biermann and C. P. Richards*) . . . 26
Theory of Electric Field on Filter Media (*W. Bergman, G. O. Nelson, H. H. Miller, R. D. Taylor and C. P. Richards*) . . . 30
Particle Size Measurement Using Laser Light Scattering (*H. H. Miller*) . . . 34
Analytical Chemistry
A Method for Determining the Percent Interference in Soil Beryllium Analysis (*N. Butterfield*) . . . 38

TECHNICAL NOTES

Radiation Protection
A Portable Hand and Shoe Counter (*C. A. Harder, T. E. Jenkins and J. W. Pregler*) . . . 39
FORIST, NE 213 Neutron Unfolding Code at LLL (*R. E. Strout II*) . . . 39
Industrial Hygiene
Study of LLL Self-Contained Breathing Apparatus Program (*B. J. Held and C. P. Richards*) . . . 40
Fire Safety
Measurements of the Combustion Heat Release Rate of Laboratory Construction Materials with a Modified Flame Spread Apparatus (*N. J. Alvares, H. W. Ford, Jr. and D. G. Beason*) . . . 41
Flammable Hazards of Christmas Trees on Display (*D. G. Beason and H. W. Ford, Jr.*) . . . 46

PUBLICATIONS 47

REFERENCES 49

Compiled by T. R. Crites
Edited by V. R. Stitt

Progress Reports

RADIATION PROTECTION

Continued Realistic Phantom Development

Introduction. Continued construction of the realistic phantom for calibration of transuranic isotope lung counters[1,2,3] is discussed in this progress report. Current work includes final shaping of the torso cast, development of a technique for making foamed plastic lungs loaded with transuranic isotopes, casting of tissue-equivalent (T.E.) organs, and acquisition of rib cages for the second and third phantoms.

Torso Cast. In the previous progress report[3] we noted that an important criterion of phantom construction is that the torso shell will have a thickness which simulates the x-ray attenuation of the chest wall of a very thin individual. Specifically, this means that the average transmission of plutonium x rays through the T.E. material overlying the lungs is equivalent to transmission through approximately 16 mm of lean soft tissue. The torso cast made from the cadaver which was the source of our first rib cage has now been altered to the necessary shape (Fig. 1). We made the alteration by vacuum forming a thin plastic replica of the torso contour. With the plastic shell in position over the plaster organ cavity cast, we mapped the space between. The difference between this space and the required "chest wall" thickness was removed from the torso cast to yield the final torso. "Chest plates" will now be made of T.E. material to overlay the phantom to simulate differences in human stature.

Lung Casting and Loading. Our Plastics Shop has prepared a formulation of commercially available polyurethane which will give us a density of 0.25 g/cm^3 which is equivalent to the nominal density of human lung. The material we use is polyurethane foam 1940D (Black) available from the CPR Division of Upjohn Corp. The recommended formulation has been altered by our Plastics Shop personnel to yield the desired density (30.0% 1940D component A, 68.4% 1940D component B, 0.15% water, and 1.45% acetone lanthanum nitrate solution). Our recent experience is that there is batch-to-batch variation in the foaming properties of the material, so specific tests must be made before use. Figure 2 shows a cast lung and silicone mold. We coat the finished lungs with a thin skin of unit density polyurethane to avoid contamination by radioactively loaded lungs.

One major concern over the foamed lungs and other polyurethane organs, for that matter, is the ability to introduce transuranic isotopes uniformly through finished organs. We now believe that can be done by dissolving the isotope in nitrate form in dry acetone, using lanthanum nitrate as a carrier. Dry acetone is important because unwanted water accelerates the polyurethane foaming process and alters the finished product. At present we are using 3 to 10 ml of acetone with up to 10% lanthanum nitrate in each lung section.

Of course, a key to the loading process is knowing that the radioactive material (essentially lanthanum) will be uniformly mixed through the lung volume. To test loading uniformity, we made a lung loaded only with lanthanum (no radioactive material). The lung was sliced along the plane having the largest cross-sectional area. Then, using a system which measures elemental

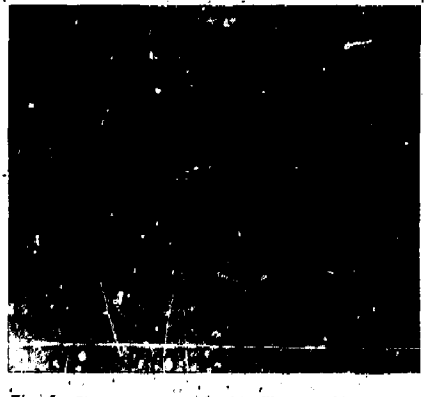

Fig. 1. Plaster torso model with silicone molds.

Fig. 2. Foamed polyurethane "lung" with silicone molds.

concentration by x-ray fluorescence, we mapped the relative concentration of lanthanum in the lung. The result is shown in Fig. 3. The measured variation in concentration of lanthanum through the organ volume is certainly acceptable for our requirements.

Organ Casts. Fabrication of the silicone molds of other major organs has been reported before.[3] We have now cast replicas using our T.E. plastic formulation (4.3% calcium carbonate; 95.7% polyurethane). Figure 4 shows the T.E. heart, kidneys and liver together with the actual organs.

New Rib Cages. We plan to build three phantoms in order to meet the needs of the transuranic measurements intercomparison program.[1] We have now obtained rib cages for use in phantoms 2 and 3. Although there are some differences, the new rib cages appear to fit well on the existing organ cavity mold. The second rib cage does present an interesting example of human anatomical variability. There is a bifurcation of the cartilage that connects the third rib on the left side to the sternum (Fig. 5). As a result, the rib itself is unusually wide at the point of cartilage attachment. This kind of aberration is not uncommon, and occurs during embryotic development. To maintain uniformity of the three phantoms, the rib will be trimmed before construction, and a normal plastic cartilage replacement will be used.

Work Remaining. Before casting the first torso, we must make cartilage-equivalent segments and attach them to the ribs and sternum. After casting a torso without ribs to test the molding process, we will make the first phantom torso. We must also make T.E. organ cavity filler for space not occupied by major organs. This will include provision for tracheal lymph nodes.

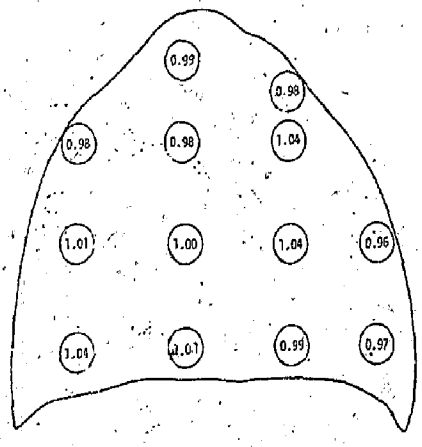

Fig. 3. Cross section of lung with map of relative lanthanum content.

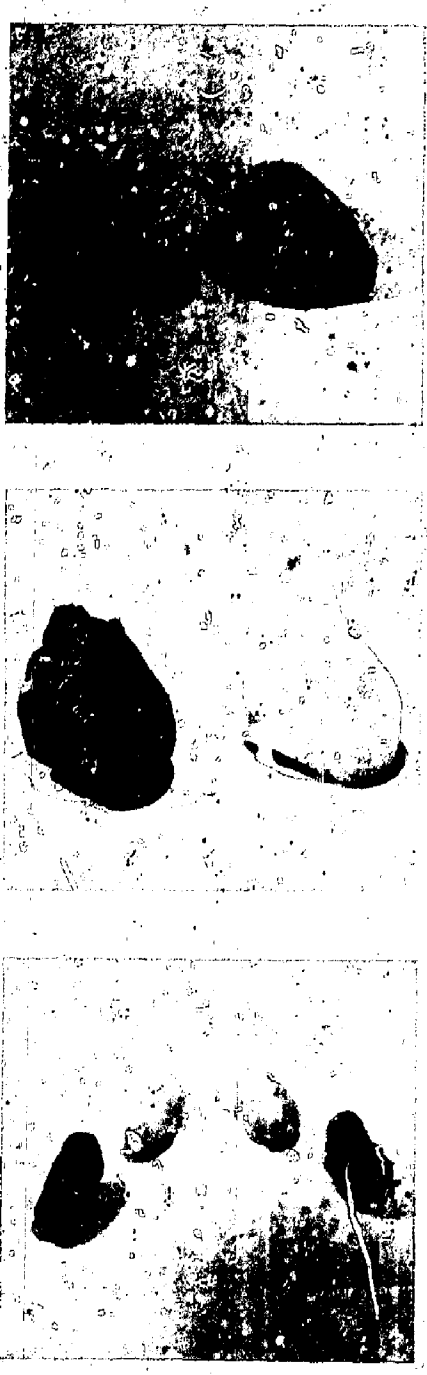

Fig. 4. Tissue-equivalent organs shown with human counterparts.
(a) Liver,
(b) heart, and
(c) kidneys.

We will make a set of unloaded lungs as well as lung sets, liver, and lymph nodes loaded with ^{238}Pu, ^{239}Pu and ^{241}Am. Finally the first phantom will be completed by casting T.E. chest plates to be placed on the phantom to simulate people having different body statures.

Acknowledgments. As usual, a number of people have contributed to this project. We would like to thank Norm Boyer, Robert Taylor, and the Plastics Shop personnel for their help and interest in all phases of the plastics work, Robert Jones at the University of California, Berkeley Campus, Museum of Vertebrate Zoology, for his help in preparing the rib cages, Ken Hulet of our Radiochemistry Division for his advice on incorporating radioactive material in the organs, and Sexton Sutherland and Jerry Ritchie at the University of California Medical Center, San Francisco, for their help in obtaining the rib cages.

Calculated Response Matrix for a Collimated 2 X 2 NaI(Tl) Gamma Ray Detector

Several small NaI(Tl) detectors are now being used at LLL to measure gamma-ray energy spectra for the purpose of determining dose rates, and to verify transport calculations. The gamma-ray continuum is of particular interest here since only a small portion of the total dose rate is due to unscattered photons. Consequently, a simple photopeak integration is inadequate for our purpose. Instead, the pulse-height response of the detectors to monoenergetic photons must be determined and unfolded from the pulse-height data to provide the full gamma-ray energy spectrum.

A code called GAMREDUX is currently under development at LLL for the purpose of unfolding gamma-ray pulse-height data. It is a successor to the GAMSPEC code[4] and uses the unfolding strategy from Mollenauer's GAMSPEC.[5] Due to the small number and limited energy range of available monoenergetic photon sources, the pulse-height response matrix cannot be determined experimentally for photon energies above about 1 MeV. The response matrix for our system is being calculated using a coupled photon-electron transport Monte Carlo code called SANDYL.[6] Upon completion of the response matrix calculation, the results will be parameterized in the form used by Berger and Selzer.[7] A set of parameter data is then used by the LLL code GAMRESP[8] (described elsewhere in this report) where a smoothed and rebinned matrix is produced for input to the GAMREDUX unfolding code.

Pulse-height response of the NaI(Tl) detector is described, using the definitions from Ref. 7. First, the response function $R(E_\gamma,h)$ is given by Eq. (1) below:

$$R(E_\gamma,h) = \eta(E_\gamma) \int_0^\infty D(E_\gamma,E_d)\, G(E_d,h)\, dE_d \qquad (1)$$

where

$R(E_\gamma,h)dh$ = probability that a gamma-ray incident on the detector with energy E_γ will produce a pulse with height between h and h + dh.

$\eta(E_\gamma)$ = probability that an incident gamma ray at energy E_γ will interact at least once in the detector.

$D(E_\gamma,E_d)dE_d$ = probability that the gamma ray, if it interacts in the detector at all, will deposit an amount of energy E_d between E_d and $E_d + dE_d$.

$G(E_d,h)dh$ = the probability that the deposition of energy E_d will give rise to a pulse with height between h and h + dh.

Then the pulse-height distribution P(h) is given by Eq. (2) below for a gamma-ray differential flux, $\phi(E)$ photons/cm^2-s-MeV:

$$P(h) = A\,T \int_0^\infty R(E_\gamma,h)\, \phi(E_\gamma)\, dE_\gamma \qquad (2)$$

where

T = length of data acquisition (s)

A = effective cross-sectional area of detector (cm^2).

Fig. 5. Close-up of human ribcage showing bifurcation in cartilage and rib.

If the pulse-height distribution is binned into several groups of width ΔE_h and the gamma-ray energy distribution is binned into groups of width ΔE_γ then Eq. (3) below relates the contents of these bins:

$$P_i = \sum_j R'_{ij} \phi_j \qquad (3)$$

where

P_i = counts in the *ith* pulse height bin,

ϕ_j = photon flux in the *jth* bin,

R'_{ij} = the detector response matrix given by Eq. (4) below:

$$R'_{ij} = AT\, \Delta E_\gamma \Delta E_h \eta_i \sum_k D_{ik}\, G_{kj} \qquad (4)$$

The purpose of the calculations described below is to arrive at an estimate of the *deposition spectrum*, $D(E_\gamma, E_d)$. This estimate is then smoothed by the resolution function, $G(E_d, h)$, and the detector response matrix R' is calculated according to Eq. (4) above.

Results to Date. Calculations for an uncollimated 3 X 3 NaI detector have been carried out and reported in Ref 7. The measurements we are currently undertaking require a collimated detector since the gamma-ray background is often very high in the area where spectral measurements are carried out, and this background varies significantly during the period of some measurements. Consequently, the collimator shown in Fig. 6 is used to reduce the detected background. However, a penalty is paid for collimation because the pulse-height response of the detection system is complicated by photon interactions in the collimator. Not only is there a significant Compton-scattered photon intensity from the collimator, but there is also bremsstrahlung radiation, lead x rays, and, for photons above 2 mc^2 there is 511 keV annihilation radiation.

At present, the pulse-height response of a 2 X 2 NaI(Tl) detector located in the collimator as shown is being calculated. For purposes of calculation the photon source is assumed to be a point, monoenergetic source with uniform angular intensity over a cone which illuminates the collimator face to a radius of 10.5 cm. The radius of illumination was restricted due to the very large machine time requirement of the coupled electron-photon problem (up to 3.5 hours per problem on a CDC 7600 system for 3 X 10^4 source photons). Photons and electrons were tracked until their energies were reduced below 50 keV, at which point their remaining energy was deposited. All bremsstrahlung and fluorescence photons were tracked, as well as photoelectric and auger electrons. Knock-on electrons were not followed. Each problem consisted of 3-5 X 10^4 source photons. Statistics were poor since only about 1000 to 1500 of these interacted in the detector. The results were th smoothed to obtain the best estimate of the *detector response*.

These calculations are not yet complete, but some of the results obtained so far are given below. Figure 7 shows a plot of P_0, P_1 and P_2 which are the fraction

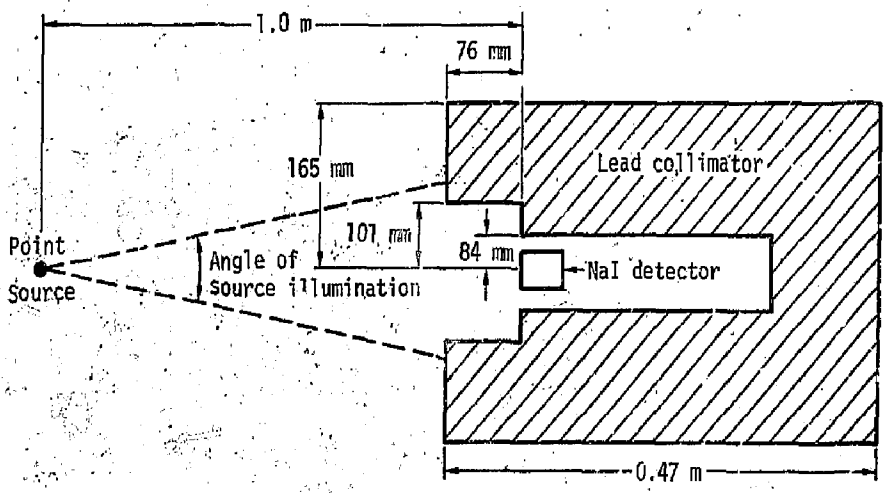

Fig. 6. Source-detector-collimator geometry.

of interactions in the detector which contribute respectively to the full energy peak (FEP), single escape peak (SEP), and double escape peak (DEP). Table 1 contains a tabulation of the same data. Values of P_0 are in good agreement with those obtained by others.[7-10]

In addition to the photo peak and escape peaks, the pulse-height spectra also exhibit a peak due to escape of iodine x-ray fluorescence photons and a peak at 511 keV due to positron annihilation occurring in the collimator for photons above 1.02 MeV. No effort has yet been made to characterize the iodine escape peak. However, the 511-keV peak has been treated in a manner analogous to the escape peaks. A parameter, P_4, is the ratio of counts in the 511-keV peak to the total number of detector counts. This is also plotted in Fig. 7.

Absolute peak efficiencies may be obtained from the product of the detector efficiency, $\eta(E_0)$, and the appropriate peak fraction parameter P_0-P_4. Total efficiency is calculated from the NaI total cross section given by Heath,[11] and is plotted for the 2 X 2 detector in Fig. 8.

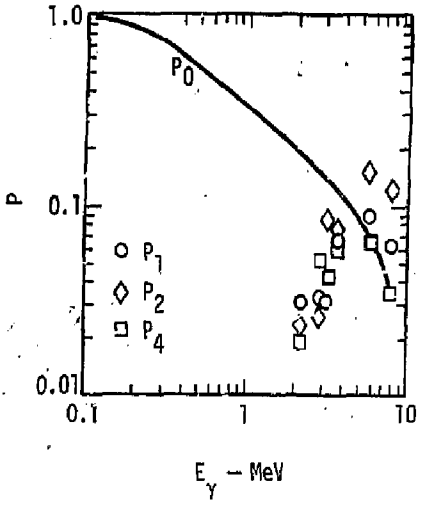

Fig. 7. Peak-to-total ratios. P_0 = full energy peak, P_1 = single escape peak, P_2 = double escape peak, P_4 = 0.511-MeV peak.

Table 1. Peak fractions for 2 X 2 NaI detector

E_γ	$\eta(E_\gamma)$	P_0	P_1	P_2	P_4
0.112 MeV	1.0	0.93			
.15	1.0	.95			
.207	1.0	.88			
.238	0.99	.85			
.295	.96	.72			
.332	.93	.71			
.351	.92	.67			
.375	.90	.65			
.413	.88	.62			
.450	.86	.59			
.511	.82	.53			
.583	.79	.48			
.609	.78	.47			
.662	.76	.46			
.727	.74	.42			
.835	.71	.38			
0.911	.70	.34			
1.001	.68	.33			
1.764	.56	.22	0.0075	0.0075	0.018
2.200	.53	.19	.029	.019	.023
2.615	.51	.17	.043	.035	.040
2.900	.50	.13	.032	.051	.027
2.23	.49	.12	.031	.044	.083
3.70	.48	.12	.066	.062	.068
4.43	.48	.090	.055	.058	.118
5.80	.48	.074	.090	.067	.152
7.66	0.49	0.037	0.063	0.035	0.125

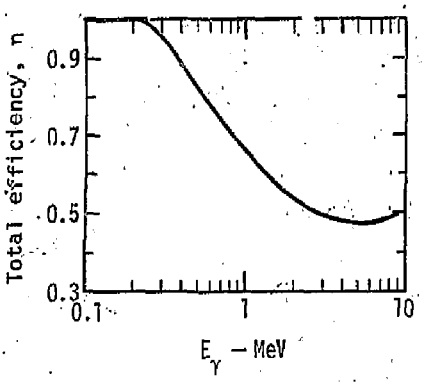

Fig. 8. Total efficiency for 2 X 2 NaI(Tl) gamma-ray detector.

Finally, Fig. 9 shows the calculated pulse-height response at selected incident photon energies. It is clear from the figure that bremsstrahlung radiation produced in the collimator is important for incident photon energies above a few MeV. A peak in the responses due to large-angle Compton scattering is also prominent for photon energies in the range 0.5 to 2 MeV.

It is clear that an inner shield, graded toward low Z materials, would be of some benefit in reducing the low pulse-height response to energetic photons. This will be studied in future calculations. Other detectors will also be studied, including a 1 X 1 and a 3 X 3 detector in the same collimator.

We anticipate calculating responses for the 1 X 1 and 2 X 2 detectors with and without collimation, and will parameterize the results for comparison with the 3 X 3 data given in Ref. 7.

Developments in a Combined Albedo Electrochemical Track Etch Personnel Neutron Dosimeter

Introduction. In previous progress reports,[12-14] we have discussed the electrochemical etch (ECE) technique and its potential use in personnel neutron dosimetry. We have presented data on the etching process, the subsurface nature of tracks, and the monoenergetic neutron response of ECE-using polycarbonate detectors. In this report we present further data on the etched track structure, the phantom-mounted response of ECE samples to distributed energy neutron sources, and use of the ECE technique in combination with albedo dosimeters for personnel neutron dosimetry.

Track Structure. The ECE process involves caustic etch of damage trails or tracks resulting from movement of heavy charged particles through a dielectric such as polycarbonate. In ECE, an ac field is applied through the sample[12] to accelerate the etching process. The result is a "treeing" effect caused by the electrical stress, so that the etched volume in the sample develops as tree-like branches with the "trunk" being the tiny surface pore which allows the etch products to be removed from the sample. As the etching proceeds the tree volume is cleaned out, leaving a large void under the film surface. The size of the volume varies from track to track, but with our etching process, (0.25-mm sample thickness, 800-V potential, 2-kHz frequency, 28% KOH at room temperature) the dosimeter is typically 0.07 to 0.1 mm in diameter after a 5-hour etch.

We have sliced some samples after etching to look at the vertical shape of the tracks. Figure 10 shows a comparison of the size and shape of typical tracks for etching periods between 2 and 5 hours. The track structure of the 2-hour track is not clear in the photo; however, it has been included for size comparison. An interesting point is that many tracks seem to have two etched volumes in line. This may result from the early etching process in the track near the surface allowing etchant to enter a second damage trail deeper in the sample.

In a recent paper[15] it has been noted that tracks etched with equal parts of ethyl alcohol and 28% KOH are much larger than those etched only in KOH solution. We etched some samples under both conditions, and the tracks using ethyl alcohol and KOH are indeed much larger than those with KOH alone. However, the background with the combination solution is also much higher, and is totally unacceptable for our purpose. It is interesting, though, to compare the track shapes from the two processes. Figure 11 shows that the combination etchant yields a track that is much more tree-shaped than tracks from the KOH alone.

Neutron Response Studies. The ECE technique with polycarbonate detectors is insensitive to neutrons below about 1.5 MeV.[13] It cannot be used as a full-energy-range dosimeter. In addition, the etching and counting process does not lend itself well to the automation required of a facility using many personnel dosimeters. It does, however, represent an attractive addition to widely used albedo dosimeters. Albedo dosimeters, though sensitive and easily automated, have a dose-equivalent response that is highly spectrum-dependent and relatively insensitive to fast neutrons. Polycarbonate foils can be added easily to many existing albedo dosimeters. If processed only when there is a positive response on the automated TLD albedo detector, they would represent a much needed fast neutron component for the dosimetry

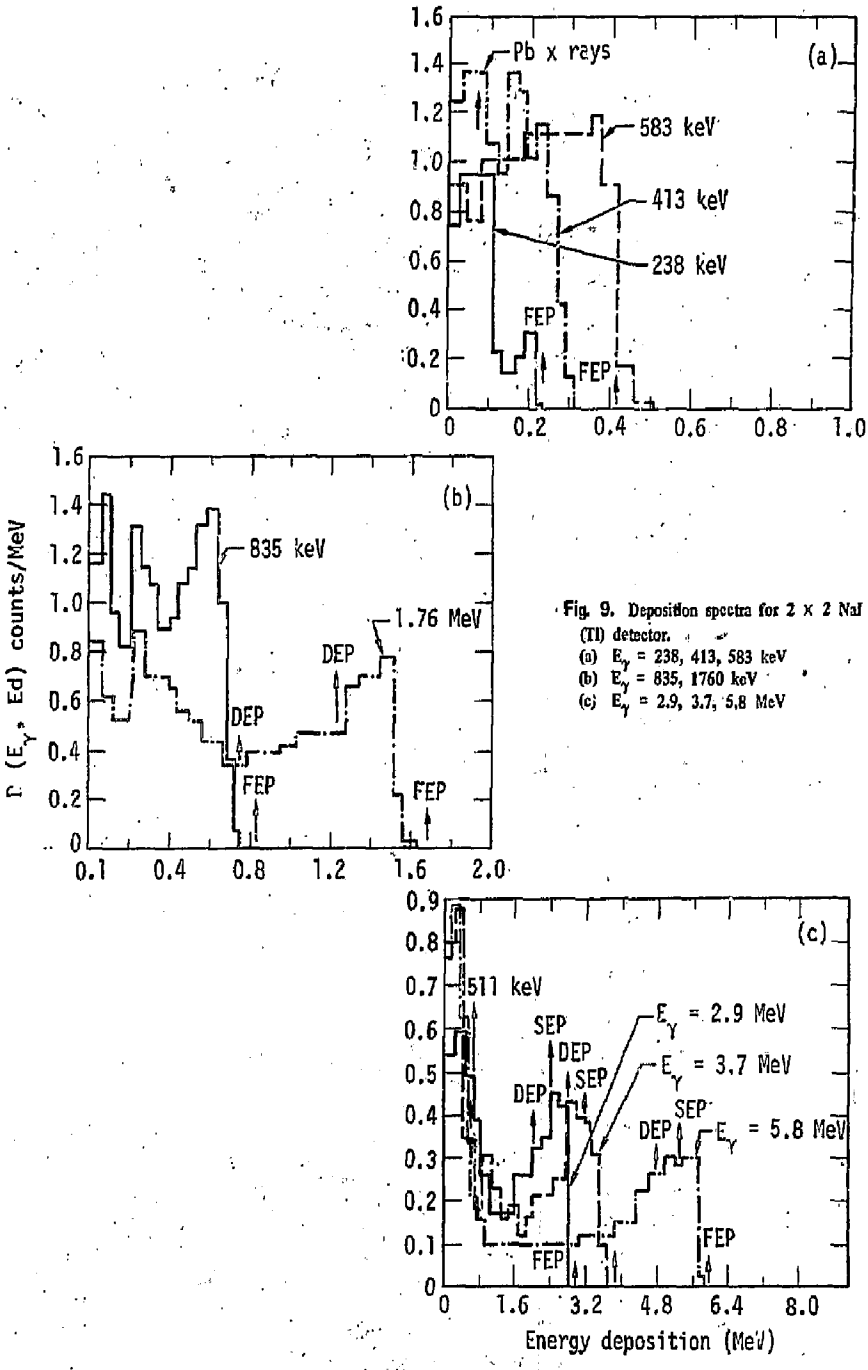

Fig. 9. Deposition spectra for 2 × 2 NaI (Tl) detector.
(a) E_γ = 238, 413, 583 keV
(b) E_γ = 835, 1760 keV
(c) E_γ = 2.9, 3.7, 5.8 MeV

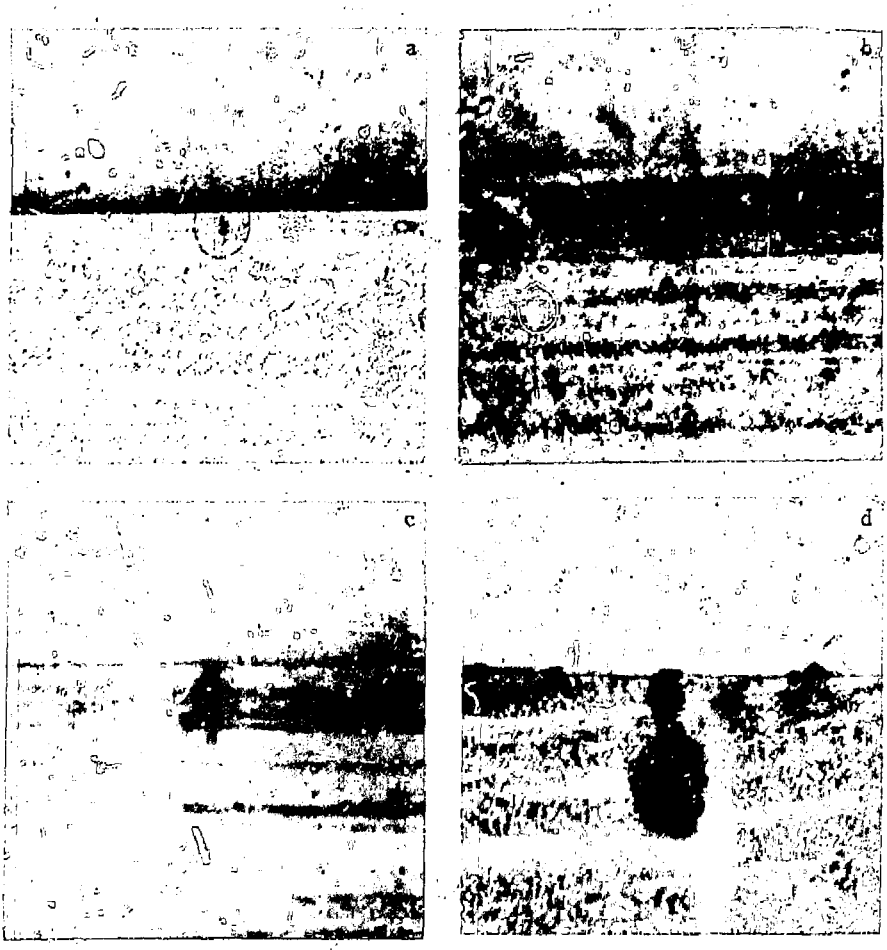

Fig. 10. Cross section of FCE tracks in polycarbonate after etch in 28% KOH, 2 kHz and 800 V (200X). (a) 2-hour etch, (b) 3-hour etch, (c) 4-hour etch, (d) 5-hour etch.

Fig. 11. Cross section of ECE tracks in polycarbonate after 4-hour etch at 2 kHz, 800 V (260X). (a) Equal parts of ethyl alcohol and 28% KOH, (b) 28% KOH.

system. In addition, we have previously shown[13] that the ratio of tracks on two sides of an ECE sample is dependent on neutron direction. Use of ECE in a personnel dosimetry could provide information on the orientation of the wearer that would be very valuable in the detailed investigation necessary following high exposures.

We have made neutron irradiations using water-filled phantoms to study the performance of a combination albedo-ECE dosimeter. Hankins-type albedo dosimeter[16] and polycarbonate samples were placed on the front and back of a stationary phantom as well as on one side of a turntable-mounted phantom that rotates at 3.7 rpm. Sets of dosimeters were irradiated with the center line of the phantom at 1 m from the source. The sources used were ^{252}Cf, $^{238}PuBe$ and 14 MeV neutron from a laboratory neutron generator. In addition, we made irradiations with the ^{252}Cf source in spherical moderators: 10-cm polyethylene, 25-cm water, 25-cm D_2O and 20-cm Al (dimensions refer to sphere radius). The dose equivalent for each irradiation was nominally 1 rem. The dose-equivalent value was taken as the average of the dose equivalent determined by multisphere measurements and discrete ordinates computer calculations.

TLD-600 from the albedo dosimeters were read and evaluated by people in our Personnel Dosimetry Group. The data have been corrected for gamma background using neutron-insensitive TLD 700 crystals. The response is presented in terms of ^{60}Co equivalent rad. The ECE samples were counted with a microscope under a magnification of 100X. Lower magnifications can be used for gross counting, but 100X is needed to see the tracks on each surface separately so we can determine incident to exit-surface-track ratio. We counted 7.2 cm^2, but ECE response is given in track density from the sum of both surfaces.

The irradiation results are summarized in Table 2. We notice that the dose-equivalent response of the albedo detectors is severely dependent on the neutron spectrum, which reflects a basic problem with that type of dosimeter. However, we can use the relationship between albedo and ECE response to predict the albedo calibration factor. In Fig. 12, the albedo response has been plotted against the ratio of ECE to albedo response. The lines represent least-squares fits calculated with a common pocket calculator. The fits have been obtained without the aluminum-moderated data because even a combined ECE-albedo system would not be able to predict the proper albedo dosimeter response to a metal-moderated source.

The fit for each set of data is of the form $\ln A = a - b \ln B$ where A is the albedo response and B is the ratio of ECE to albedo response. Table 3 summarizes the values of a and b. It is interesting, but not too surprising, to note that the slopes of the lines fitting response of the rotating phantom and the front-mounted dosimeter on the stationary phantom are almost the same. This is because almost all of the ECE response on the moving phantom occurs when the phantom faces the source. The fits described here are simple and are intended to demonstrate a relationship. More detailed work will be needed to define the proper relationship.

If we were to use the data on the three curves accurately, we need to know the geometric condition of exposure. Information to help on this problem is available from the ratio of incident to exit-surface-track densities on the ECE foils. Table 4 summarizes the values of R, the ratio of air-side to phantom-side track density on the phantom-mounted detectors. For fission or moderated spectra, R is clearly greater than 1.25 for frontal exposures and less than 0.5 if irradiated from the rear. For neutrons above about 5 MeV, the differences become less clear. A ratio of about one for fission-generated neutrons would suggest that the exposure was more isotropic than unidirectional.

Summary. The data presented here strongly suggest that addition of the fast neutron sensitive ECE polycarbonate detectors to an albedo personnel dosimeter can improve our ability to estimate the dose equivalent received by the wearer. The ECE provides a second detector with a significantly different response than the albedo badge so that an estimate of spectral quality becomes available. In addition, ECE provides orientation information not otherwise available. Of course, other fast neutron detectors such as NTA film or fission tract detectors would also improve the use of albedo dosimeters, but lack the ability to determine orientation.

Acknowledgments. I wish to thank Leroy Davis of our Special Projects Division for etching the ECE samples, Dale Hankins of our Radiation Safety Division for his help with use of the albedo dosimeters, Carl Sundbeck of Radiation Safety for processing the albedo dosimeters, and Wade Patterson for the computer-calculated dose-equivalent estimates.

GAMRESP: A Computer Code to Calculate NaI(Tl) Gamma Detector Response Matrices

We have written a program to calculate NaI detector responses using parameterized response tables as discussed by Berger and Seltzer.[17] The parameter tables account for escape peaks, iodine and x-ray escape, multiple scattering, and bremsstrahlung.

Table 2. Response of albedo and electrochemical etch (ECE) polycarbonate detectors to distributed energy neutron sources

Source	ECEP[a] Tracks cm^{-2} rem^{-1}			Albedo Rad[b] rem^{-1}		
	Phantom orientation			Phantom orientation		
	Front	Rotating	Rear	Front	Rotating	Rear
^{252}Cf	47	11.9	3.5	0.151	0.098	0.059
Cf in 10 cm CH_2	32	14.7	3.3	0.55	0.30	0.088
Cf in 25 cm H_2O	42	17.8	6.1	0.43	0.234	0.080
Cf in 25 cm D_2O	23	8.0	18	3.4	1.81	0.239
Cf in 20 cm Al	14	3.7	1.3	0.28	0.158	0.070
^{238}PuBe	97	31	15	0.192	0.079	0.069
14 MeV	94	41	30	0.042	0.031	0.035

[a]Background – 1.1 tracks · cm^{-2}.
[b]Rad response based on a ^{60}Co calibration.

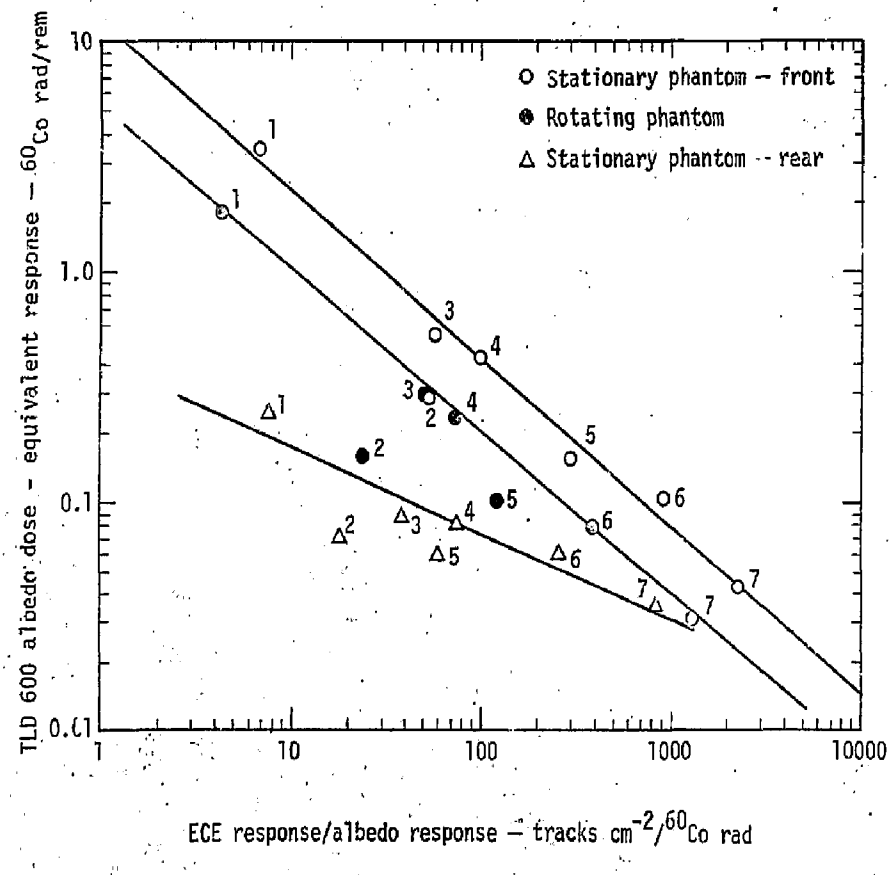

Fig. 12. Albedo dosimeter dose equivalent response as a function of ECE-to-albedo response ratio. 1. Cf – 25 cm D_2O, 2. Cf – 20 cm Al, 3. Cf – 10 cm CH_2, 4. Cf – 25 cm H_2O, 5. ^{252}Cf, 6. PuBe, 7. 14 MeV.

GAMRESP calculates the response at a series of input deposition energies for each source energy as

$$R(E_\gamma,E_d) = \eta(E_\gamma) \times \int_{-\infty}^{\infty} D(E_\gamma,E_d)\, G(E_d,E_d - E_{d'})\, dE_{d'}, \quad (5)$$

where:

- $R(E_\gamma,E_d)$ is the final calculated detector response matrix in counts/MeV per unit incident flux,
- $\eta(E_\gamma)$ is the probability that the incident gamma ray will have at least one interaction in the detector,
- $D(E_\gamma,E_d)$ is the probability that the gamma ray will deposit an amount of energy between E_d and $E_d + \Delta E_d$,
- $G(E_d,E_d - E_{d'})$ is the Gaussian smoothing function to distribute the response spectrum to the proper resolution of a particular detector,
- E_γ is the input array of source energies,
- E_d is the input array of deposition energies (one array per source energy).

An intermediate response $R(E_\gamma,E_b)$ is calculated using 200 equally spaced energy points, E_b, up to E_γ.

$D(E_\gamma,E_b)$ is calculated in two parts. First, the appropriate intensities are placed at E_γ, E_γ-mc^2, E_γ-$2mc^2$, and E_γ-29 keV when applicable. The peak values are chosen by interpolation from a peak parameter table. Second, the Compton continuum is added to the spectra. Each point is found by interpolation of a continuum parameter table. The peak and continuum parameter tables are normalized to give response in units of counts per incident photon. The response spectrum is next multiplied by efficiency $[\eta(E_\gamma)]$ at E_γ. Efficiencies were obtained from the polynomial:

$$\eta(E_\gamma) = 0.8 - 0.423 \log_{10} E_\gamma + 0.076 (\log_{10} E_\gamma)^2 + 0.309 (\log_{10} E_\gamma)^3 - 0.118 (\log_{10} E_\gamma)^4 \qquad E_\gamma \geq 200 \text{ keV} \quad (6)$$

$$\eta(E_\gamma) = 1.0 \qquad E_\gamma \leq 200 \text{ keV} \quad (7)$$

This polynomial was obtained by fitting a table of 3 X 3 efficiency values.[17]

$G(E_d,E_d - E_{d'})$ is the Gaussian smoothing function applied to $R(E_\gamma,E_b)$. The resolution (FWHM) of the Gaussian is determined from the input parameter $R_{0.661}$ (resolution of the detector at 0.661 MeV) by the relation in Ref. 17,

$$\text{Resolution} = R_{0.661}\, (0.661/E_b)^{0.34}.$$

The Gaussian smooth retains the area to within 1%.

The final smoothed response $R(E_\gamma,E_d)$ is constructed by interpolation from $R(E_\gamma,E_b)$. The array E_γ and the matrix E_d may be input or calculated internally.

Table 3. Constants for the equation ln A = (a - b) ln B

	a	b
Stationary phantom, front	2.53	0.736
Rotating phantom	1.61	0.705
Stationary phantom, rear	-0.941	0.369

Table 4. Ratio of track density on air side to phantom side of ECE polycarbonate samples

Source	Stationary phantom		Rotating phantom
	Front	Rear	R
^{252}Cf	1.7	0.4	1.9
Cf in 10 cm CH_2	2.0	0.3	1.5
Cf in 25 cm H_2O	1.3	0.4	0.8
Cf in 25 cm D_2O	1.8	0.2	0.9
Cf in Al	2.1	0.2	0.8
$^{238}PuBe$	1.6	0.7	1.8
14 MeV	1.0	0.8	0.9

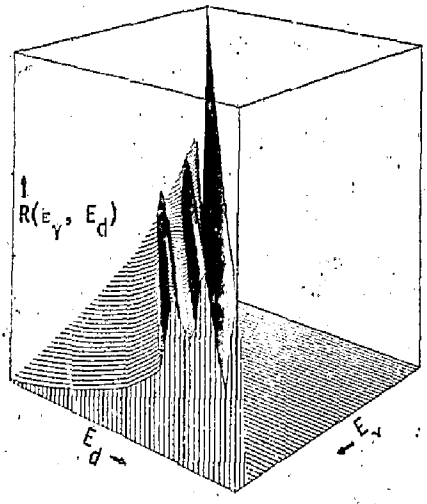

Fig. 13. 3D plot of calculated 50 X 50 response matrix.

A plotting package is included in the code to display the response in various configurations.

Figure 13 shows a three-dimensional log plot of a calculated 50 X 50 response matrix.

$$1\ MeV < E_\gamma < 10\ MeV \quad 1\ MeV < E_d < 10\ MeV$$

In this case, equally spaced values of E_γ and E_d were chosen for ease of plotting.

If desired, any set of E_γ and E_d may be chosen in the range of 50 keV to 10 MeV. Any size matrix may be chosen (even non-square) up to 100 X 100.

At this writing, only the peak and continuum parameter tables in Berger and Seltzer[17] are being used, but a photon transport code SANDYL is being run to calculate peak and continuum parameter tables for 1 X 1 and 2 X 2 NaI detectors with various geometries, and will be incorporated into the code.

INDUSTRIAL HYGIENE

Performance Reliability of Self-Contained Breathing Apparatus Exposed (Stored) to Various Temperatures

Introduction

This study was undertaken to determine the adverse effects of storing self-contained breathing apparatus (SCBA) in temperature extremes that can occur in the diverse operations of Hazards Control. For example, Fire Department SCBA is stored in compartments located on the fire engines (or on trucks) at the Livermore site and at Site 300. This equipment is exposed to ambient air temperatures in excess of 37.8°C (100°F). At the Hoe Creek Coal Gasification site in Wyoming, SCBA have been stored in unheated buildings that during the winter months reach temperatures of -46°C (-50°F). Temperatures of -46°C (-50°F) are also experienced during air shipment of SCBA in unheated aircraft cargo holds.

It is suspected that environmental temperatures may be related to maintenance problems experienced by the Respirator Branch of Hazards Control, and to malfunctions found occasionally at field sites. Maintenance of facepieces (facepiece lense sealing and rubber deterioration) is unusually high at the Livermore site and Site 300. Air cylinder leakage has been found in SCBA stored at the Hoe Creek operation and those shipped by air freight.

To isolate and identify the effects of temperature, complete fully charged SCBA were placed in an environmental chamber with controlled temperatures and humidity for definite time periods. A visual inspection of the apparatus and the major components was made after each exposure. The device was then donned and operated to make a subjective analysis of performance.

The SCBA tested were as follows:

- Scott Air Pak (6000 series)
- Scott Air Pak II (9000 series)
- MSA Air Mask 401 w/Clearvue facepiece
- MSA Air Mask 401 w/Ultravue facepiece (silicone)
- MSA Air Mask 401 w/Ultravue facepiece (Hycar rubber)
- U.S. Diver's Survivair (silicone facepiece)
- U.S. Diver's Survivair (neoprene rubber facepeice)
- Robert Shaw (formerly Lear Siegler) 5-minute escape capsule

Cold Storage SCBA Test

Visual Inspection. Each of the SCBA were placed in the environmental chamber and exposed for 24 hours at -32°C (-25°F). After the exposure, each device was examined for defects, and the following observations were noted for each SCBA configuration:

- Scott Air Pak (6000 series)
  - air cylinder empty (part No. 6102-1, ICC No. 3AA-2015)

- exhalation valve diaphragm collapsed and frozen
- regulator valves frozen shut
- lense shattered when accidentally dropped
- facepiece very rigid (hard), edges sharp

Figure 14 demonstrates the friability of the Scott 6000 series facepiece lense when stored at -32°C (-25°F). The facepiece on the left shattered when accidentally dropped during examination. The other facepiece was deliberately dropped to verify the friability of the lense material.

- Scott Air Pak II (9000 series)
  - air cylinder leak (600-lb pressure loss)
  - air leak at inlet to regulator
  - exhalation valve diaphragm collapsed
  - facepiece very rigid (hard)
- MSA Air Mask 401 w/Clearvue facepiece
  - breathing tube very rigid, low flexibility
  - main line valve leakage at regulator
- MSA Air Mask 401 w/Ultravue facepiece (silicone)
  - breathing tube very rigid
  - regulator control valves (main and bypass) hard to operate
- MSA Air Mask 401 w/Ultravue facepiece (Hycar rubber)
  - breathing tube very rigid
- U.S. Diver's Survivair (silicone facepiece)
  - nosecup valves unattached (see Fig. 15)
  - breathing tube rigid
- U.S. Diver's Survivair (neoprene rubber facepiece)
  - facepiece edges sharp and stiff
  - breathing tube rigid
- Robert Shaw (formerly Lear Siegler) 5-minute escape capsule
  - hood stiff
  - hood breathing tube connection brittle, breaks easily when unfolding

Figure 16 illustrates the breakage experienced when we tried to unfold the air capsule stored at -32°C (-25°F). The breakage occurred where the breathing tube adapter is fixed (heat-sealed) to the plastic hood.

Donning Test. After a 2-minute visual inspection, each unit was donned by an experienced SCBA user to determine facepiece fit during an irritant smoke tube test. Fitting quality is summarized in Table 5.

The test subject experienced noticeable throat and chest discomfort while breathing the chilled, dry compressed air. As a result of this, the wearing time of each unit was limited to 3-4 minutes. This discomfort made it difficult to assess accurately what was described (by the test subject) as sensation of restricted air flow and increased exhalation resistance. These factors will be further examined with instrumented bench test procedures, using a breathing simulator, during the next quarter.

Additional tests will be conducted to determine the frequency and cause of air cylinder leakage due to cold temperature exposures.

For the present time it is recommended that SCBA air cylinders, air shipped and/or stored at sites with temperatures below 0.0°C (32°F) be inspected on arrival or daily when such a condition exists.

Hot Storage SCBA Test

The SCBA were exposed to ambient air temperatures of 65.6°C (150°F) and 93.3°C (200°F) for one-half hour each, and donned by experienced SCBA users. The exposure duration was limited, and it was not determined if the SCBA components reached temperature equilibrium. A lack of information and experience with these exposure temperatures dictated that a prudent policy of caution be followed. The results, subjective in nature, identified the potential (and some real) problems that are to be examined more thoroughly with instrumented test procedures using a breathing simulator.

In general, it was observed by the test subject that the black-colored facepieces, particularly those having the greatest mass (and accordingly the highest degree of heat retention) were the most uncomfortable upon contact with the face. The lighter weight and lighter colored (blue and yellow) silicone facepieces did not give this impression. All of the facepieces except the

Fig. 14. Scott 6000 Series masks stored at -32°C.

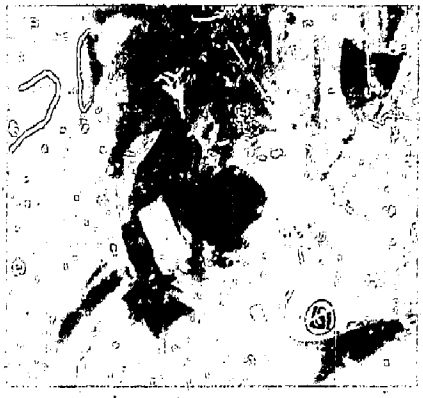

Fig. 15. U.S. diver's Survivair with silicone facepiece.

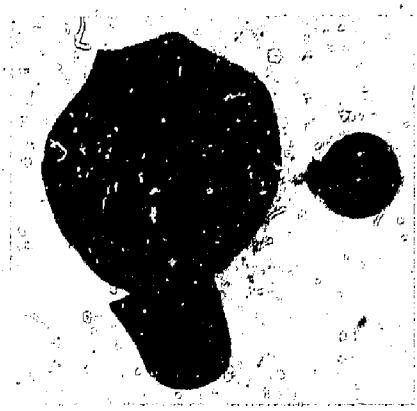

Fig. 16. Robert Shaw 5-minute escape capsule.

Scott Air Pak (6000 series) were more flexible at these high temperatures, and appeared to fit with less head harness tension. The Scott Air Pak (6000 series) facepiece lense flattened out at the 65.6°C (150°F) exposure level, causing the lense and facepiece to separate. It should be noted that most of the SCBA manufacturers warn against exposing facepieces to temperatures above 140°F. However, this is not an uncommon experience for a fireman fighting a routine fire for periods of 10 to 15 minutes. At higher temperature, most facepiece lense material (plastics) will return to the shape (flat sheets) in which it was originally manufactured.

The silicone headbands of the silicone facepiece Survivair SCBA unit become softened at 65.6°C (150°F) and slip through the retaining buckles on the facepiece, preventing the facepiece from fitting firmly. The shore durometer number (softness) of silicone decreases with increasing temperature at a rapid rate, making it an undesirable material for use as a head harness where it is necessary to maintain a steady tension. The neoprene and Hycar rubber head harness material did not exhibit any noticeable softening and/or slippage.

It is recommended that all facepieces (silicone or rubber) be equipped with neoprene or rubber-blended head harnesses for reliability at all temperatures and greater overall durability.

All of the SCBA tested demonstrated a tendency for the breathing regulators to be increasingly noisy as the air temperature at which they were stored increased. This characteristic is believed to result from softening and stretching of the breathing diaphragm housed in the regulator. The noisier regulators were those having silicone rubber breathing diaphragms. This noise (honking) interfered with the user's ability to communicate.

Breathing tubes (all were made of rubber compounds) of all devices tested at above ambient temperatures (65.6°C and 93.3°C) softened and

Table 5. Fitting quality of SCBA facepieces equilibrated to -32°C (-25°F). Test medium: MSA irritant smoke tube[a]

Facepiece tested	Qualitative fit test result	Wearer's comments
Scott Air Pak 6000 series	Leak	Extremely uncomfortable Rigid, sharp edges Regulator noisy
Scott Air Pak II 9000 series	Leak	Rigid Regulator noisy
MSA Air Mask 401/Clearvue	No leak	Difficult exhalation
MSA Air Mask 401/Ultravue (silicone)	No leak	Difficult exhalation
MSA Air Mask 401/Ultravue (Hycar rubber)	No leak	Difficult exhalation
U.S. Diver's Survivair (silicone facepiece)	No leak	Regulator noisy
U.S. Diver's Survivair (neoprene facepiece)	No leak	Regulator noisy
Robert Shaw 5-minute escape capsule	Inoperable	–

[a]The test subject passed the irritant smoke tube fit test with all the SCBA equilibrated to room temperature.

stretched considerably. This suggests that the airflow characteristics of the air supply regulator may be reduced in volume, resulting in an increased inhalation resistance for the user and accordingly, a potentially higher rate of facepiece leakage.

The most obvious conclusion drawn from these qualitative heat exposure tests of SCBA is that the construction materials of the SCBA components are the limiting factors in the reliability and safety of the device. Laboratory test methods are now under development to establish the stability of individual components and operating reliability of SCBA exposed to heat stress (air temperature and radiant heat). The components to be tested individually are as follows:

- Facepiece body
- Head harness
- Facepiece lense (and lense covers)
- Exhalation (and inhalation) valves
- Nose cup
- Spectacle mounts
- Breathing tubes and fittings
- Regulator housing
  - breathing diaphragm
  - internal seals (O-rings, washers, etc.)
- Back-pack harness materials (belting, buckles, fasteners)
- High-pressure hose assembly
- Air-cylinder valve assembly
- Surface finishes (paints, plastics, etc.)

Initial tests using the radiant heat source from the NFPA #258 test procedure will be performed with each of the above components at increasing increments from 0.1 to 3.0 g cal/cm^2/s. Air temperature studies will be conducted over a range of 65.6°C (150°F) to 1000°C (1800°F). These parameters reflect the normal to extreme thermal environments encountered in fire service operations.

SCBA Communications Study

Purpose. This study was conducted to analyze and evaluate the voice transmission quality of the SCBA full-face masks for fire service and emergency applications. The nine SCBA/full-face mask combinations listed below comprise the brands and configurations tested.

- Scott Air Pak 4.5
- Scott Air Pak – 6000 series
- Scott Air Pak II – 9000 series
- MSA 401 Air Mask
  - Ultravue facepiece (silicone)
  - Ultravue facepiece (Hycar rubber)
  - Clearvue facepiece
- U.S. Diver's Survivair
  - silicone facepiece
  - neoprene facepiece
- Globe Guardsman/Sierra facepiece

In addition to evaluating the SCBA voice transmission, another series of tests was conducted to examine the techniques (use practices) by which hand-held transceivers can be used effectively by SCBA users.

Voice Transmission Clarity versus Distance. This test series was performed by donning the complete SCBA and recording the normal talking voice of subjects reading a script at increasing distances from the microphone. Evaluating the transmission was accomplished by listening to a playback of the recording and rating the transmission clarity. Recording and playback amplification of the tape recorder was held constant. The test subjects read the script at a normal talking sound level. For the first recitation, the microphone was held against the lense, for the second test at 25 mm in front of the facepiece and finally directly in front of the test subject at a distance of 0.3 m.

Table 6 lists the voice transmission clarity ratings as judged by listening to the playback of the tape recorder. A rating of 1.0 is the highest and indicates total clarity; 2.0 is audible or understandable with either resonance or muffling; 3.0 means barely audible, resonant and/or muffled but understandable; 4.0 – barely audible, resonant and muffled, requires effort; and 5.0 – totally inaudible. The ambient noise level for these tests was 70 ± 2 dBC.

All of the facepieces provided audible voice transmission when the microphone was held in contact with the facepiece lense. There was, however, a noticeable resonance (vibration) from the lense of the 6000 and 9000 series Scott facepieces. The silicone Survivair facepiece had a noticeable resonance, while the neoprene Survivair did not. This suggests that perhaps the facepiece body of the neoprene Survivair provides a more stable support for the lense.

When the microphone was held at a distance of 25 mm, all of the facepieces were able to transmit voice with clarity, except for the Scott Aviation 6000 series. The Scott 6000 had a decided resonance that reduced clarity significantly; however, it was audible.

At a distance of 0.3 m (with a 70 ± 2 dBC background), the Scott 6000 was muffled and inaudible. The Scott 9000 was also muffled, but occasional words or phrases were audible. The silicone Survivair was barely audible.

The only facepiece to transmit voice audibly at a 0.3-m distance was the MSA Ultravue, which is the only facepiece tested that has a built-in speaking diaphragm. The value of the speaking diaphragm is very evident on recordings made at a distance of 0.3 m.

This test series indicates that the heavier facepieces (Scott 6000 and 9000) are least desirable from a

Table 6. SCBA voice transmission clarity rating

SCBA	Facepiece	Transmission clarity rating[a] Contact[b]	25 mm[c]	0.3 m[d]	Comments
Scott Air Pak	6000 series	2.0	2.0	5.0	Noticeable muffled transmission at 10 ft
Scott Air Pak II	9000 series	2.0	2.0	5.0	Muffled occasionally inaudible at 10 ft
Scott Air Pak 4.5	4.5 series	1.0	1.0	3.0	Muffled and resonant at 10 ft
MSA 401 Air Mask	Ultravue (silicone)	1.0	1.0	2.0	Some resonance at 10 ft
	Ultravue (Hycar)	1.0	1.0	2.0	Some resonance at 10 ft
	Clearvue	1.0	1.0	3.0	At 10 ft clear but low volume, some muffling
Survivair	Silicone	2.0	1.0	3.0	Resonance and muffled at 10 ft
	Neoprene	1.0	1.0	2.0	Muffled but clear
Globe Guardsman	Sierra (neoprene)	1.0	1.0	2.0	Muffled but clear

Voice *Transmission Rating Method* (1.0 is highest rating).

1.0 Audible – clear and distinct, no difficulty to understand.

2.0 Audible – slightly resonant or muffled.

3.0 Barely audible – resonant and/or muffled but understandable.

4.0 Barely audible with effort – muffled and resonant.

5.0 Inaudible – not understandable.

[a]Average of two ratings.

[b]Microphone held against the lense.

[c]Microphone held 25 mm from facepiece.

[d]Microphone set in place 0.3 m from subject.

communications standpoint. With the Scott Air Pak 4.5, the voice is definitely more audible than with its predecessors (6000 and 9000 facepieces), but is not as audible as with the MSA Ultravue equipped with a speaking diaphragm. The Scott 4.5 facepiece appears to be equal to the Globe Guardsman, Survivair, and MSA Clearvue facepiece with respect to voice transmission quality.

This test series suggested that it is possible to use radio communications with SCBA facepieces provided that the transceiver is held against the lense of the facepiece. To examine this method of operation, further tests were conducted: (1) holding the microphone 25 mm in front of the facepiece, and (2) holding the microphone against the lense while maintaining a noise level background of 90 dBC.

With all of the SCBA facepieces with the exception of the MSA Ultravue (with a built-in speaking diaphragm) the voice was inaudible with the microphone held 25 mm from the facepiece. The voice was clearly audible above the 90-dBC noise background with the MSA Ultravue facepiece.

With the microphone held directly against the lense of the facepiece, all of the SCBA units were able to transmit audibly despite the 90-dBC background.

Field tests were conducted with fire service personnel (LLL Fire Department) and field radios to evaluate the technique of holding the microphone in contact with the facepiece lense. It was found that by removing the protective leather case and holding the two-way radios directly against the lense, effective radio communication was readily achieved.

INSTRUMENT DEVELOPMENT

Neutron Spectroscopy in the Energy Range 0.5-20 MeV Using a NE 213 Scintillator

Introduction. Several earlier progress reports[18-20] have described our effort to make neutron spectral measurements in the field. For neutron energies in the range 0.5-3 MeV, data have been obtained using a combination of hydrogen proportional counters and ^{3}He proportional counters. Liquid scintillation detectors (NE 213) were used in the energy range 2-20 MeV. We have met with very limited success in the past because of the low sensitivity of the proportional counters, the variability of the ^{3}He response functions with counting conditions, and the limited useful energy range of the scintillators.

Liquid scintillation detectors are capable of high sensitivity and, with good pulse-shape discrimination

(PSD) to suppress analysis of gamma ray interactions, have a highly reproducible response. Recent improvements in our pulse-shape discrimination system have extended the useful energy range of the NE 213 detectors to 0.5-20 MeV. As a result, reliable field measurements may be made over this range with a single highly sensitive detector. These data, together with those obtained using a single large hydrogen proportional counter, allow field measurements of neutron spectra over the energy range 0.05-20 MeV at neutron intensities which yield a total dose rate greater than about 0.2 mR/hr.

Neutrons interact in a NE 213 detector by elastic scattering with the hydrogen and carbon nuclei in the organic liquid. Recoil protons cause the liquid to scintillate, and the light output is detected by a photomultiplier tube. Unfortunately, the relation between recoil proton energy and light output is highly nonlinear. Consequently, the light output due to protons whose energies are in the range 0.5-20 MeV varies over the range 0.004-1.0, a dynamic range of about 250:1. Our previous PSD system[20] performed reliably only over a dynamic range of about 20:1 so that neutron and gamma interactions were not distinguished at neutron energies below about 2 MeV. Recent improvements, described below, have increased the dynamic range to 250:1.

An Improved PSD System. Figure 17 shows a block diagram of the PSD system currently in use.

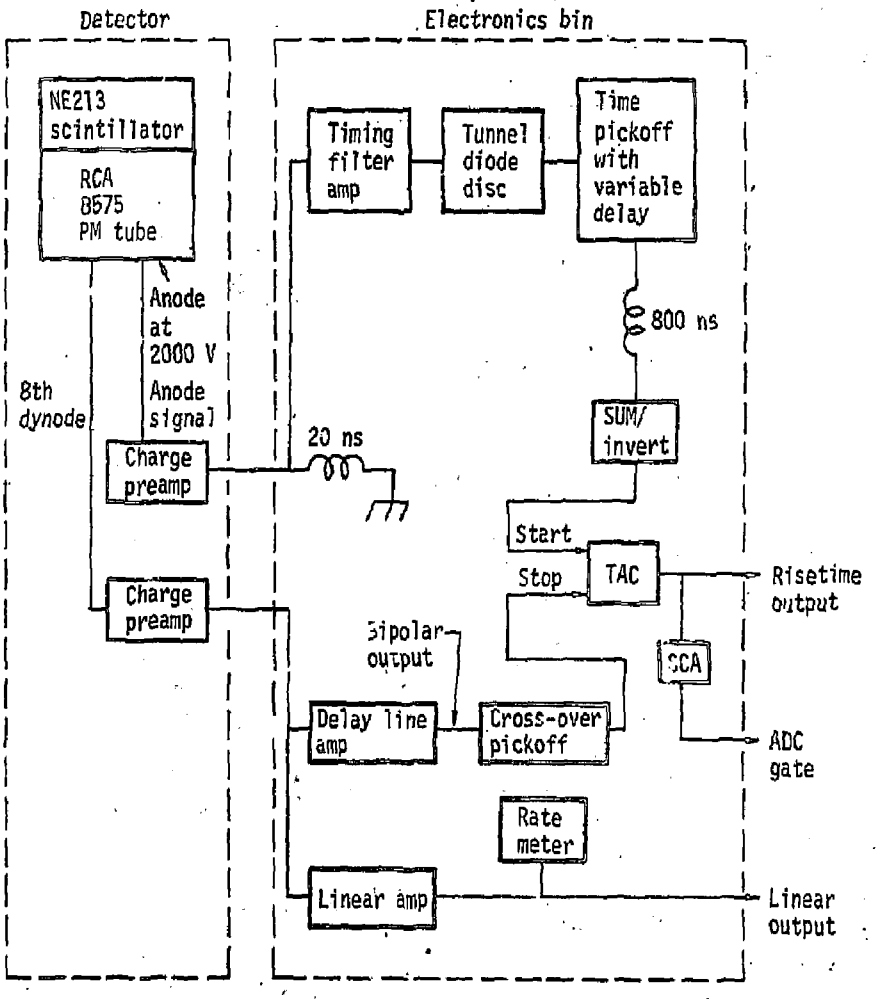

Fig. 17. NE 213 spectrometer system.

Commercially available NIM modules have been used wherever possible. The most significant difference between this system and its predecessors is the use of crossover timing rather than direct decay or risetime measurement. A linear signal developed at a very early dynode on the RCA 8575 photomultiplier is double-delay line shaped, and crossover timing is used to distinguish neutron and gamma-ray interactions. Pulse shape is determined by analyzing the time difference between the start of the light output (detected at the anode of the PM tube) and the zero crossing of the double-delay-line shaped linear signal, using a time-to-amplitude-converter (TAC). Thus, the TAC output is related directly to the risetime of the linear signal. Expansion of the risetime range is obtained by delaying the TAC start signal about 800 ns and increasing the TAC gain so that time differences on the order of 50 ns produce maximum output.

Optimum n-γ discrimination is obtained when the anode of the PM tube is driven to saturation, producing an output with a steep leading edge. This requires that 2000 V be applied. The anode signal is then matched to the low impedance transmission line using a preamplifier. A charge-sensitive preamplifier was chosen because of its low noise. The preamplifier output is terminated in a shorted 20-ns length of cable which returns the output to baseline. This signal is amplified in a timing-filter-amplifier operated at near-minimum gain to prevent spurious start signals due to overload pulses. A tunnel diode discriminator senses the start of the anode signal and produces a signal which, after suitable delay and inversion, is used to start the TAC. It is important to not allow the timing filter amplifier to be driven to overload since its recovery from overload is slow and accompanied by spurious outputs. For field work, great attention must be paid to the temperature stability of the 800-ns delay line and the dc level at the input to the tunnel diode discriminator.

The linear signal is derived from the eighth dynode of the PM tube as succeeding dynodes are observed to produce nonlinear output for the largest light pulses. A charge-sensitive preamplifier is used to increase the signal-to-noise ratio on the transmission line and for impedance matching. The linear output is passed through a double-delay-line amplifier producing a bipolar output whose zero crossing is detected by the crossover pickoff. At the time of crossover, the TAC is stopped and an output is generated which is proportional to the time interval between start and stop pulses.

Linear signals are also Gaussian-shaped for pulse-height analysis. This allows system gain changes to be accomplished easily, without retuning the PSD system. In addition, the Gaussian-shaped output provides better linearity in the pulse-height spectrum and relative freedom from spurious signals due to overload when compared to our earlier configurations.

Conclusion. A system whose configuration is shown in Fig. 17 has been used for both laboratory and field measurements of neutron spectra. Laboratory measurements have been made routinely in the energy range 0.5-20 MeV, and our experience has shown the system to be reliable. Field measurements have proven more difficult. Temperature variations from 0-43°C have caused failures, and frequently cause drift in the dc levels as well as in the delay lines. Use of RG-58 coaxial cable for the delay lines has reduced the drift in the crossover time distribution, but this remains a significant concern. Drift in the dc levels has been reduced through the use of capacitor coupling to isolate system modules.

Transmission Anode X-Ray Tube Development

The development program for transmission anode x-ray tubes (TRAX)[21-23] has recently concentrated on characterizing the performance of sputtered targets, as compared to metallic foil targets. As reported earlier,[24,25] sputtered targets offer several advantages over foils: (1) better heat dissipation, (2) better mechanical stability (freedom from "oil-canning"), and (3) the availability of target elements that are unavailable as foils. However, we suspected that the physical separation of the beam spot from the filter/converter foil and the massive beryllium support might well degrade beam purity and intensity.

To resolve these questions, two silver target tubes were constructed – one sputtered, one foil – and their performance was carefully measured. The following parameters were observed:

1. Intensity versus accelerating voltage and current
2. Intensity versus distance, with a variety of collimators
3. Beam purity, with a variety of external filters
4. Beam uniformity
5. Vacuum performance

Figure 18 shows beam intensity, in mR/min/100 μA, for both tubes, each with various external filters and operated at several voltages. Note that with little or no filtration the foil tube has higher intensity, but that as filtration is increased the difference decreases until, with the most severe filter, the sputtered target is slightly higher. This phenomenon, as yet, is not explained; however, it makes little practical difference in tube use.

Beam intensity varies with distance, of course; Fig. 19 shows typical dose rate versus intensity curves

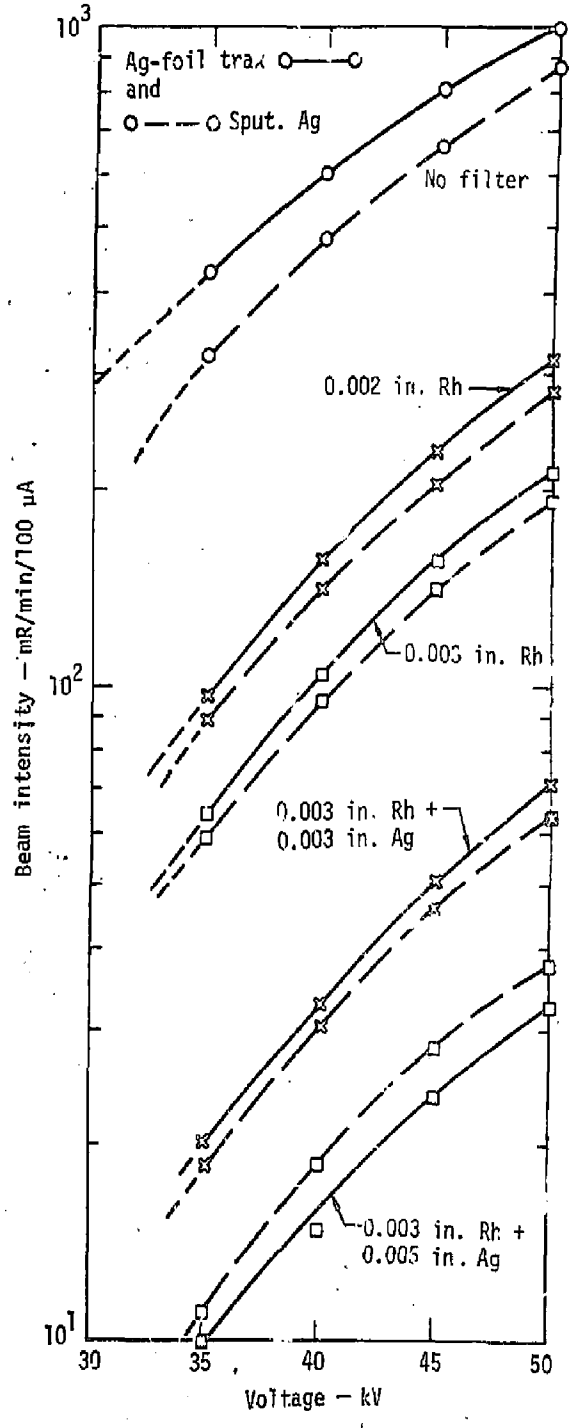

Fig. 18. Total intensity versus HV for several external filters.

for both tubes. Intensity also varies with collimator size. This is due to the intensity contribution from scattered radiation. Since the input end of the collimator is quite close to the target, small changes in the collimator diameter make fairly large changes in the number of photons which enter it. A considerable fraction of these are then scattered into the useful beam. At these low energies, the coherent

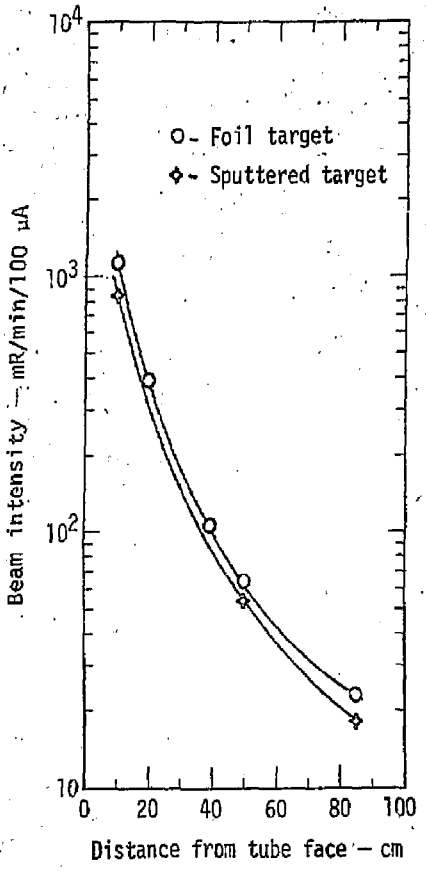

Fig. 19. Intensity versus distance, silver target TRAX 50 kV, no external filter, (0.5 x 1 in.) collimator.

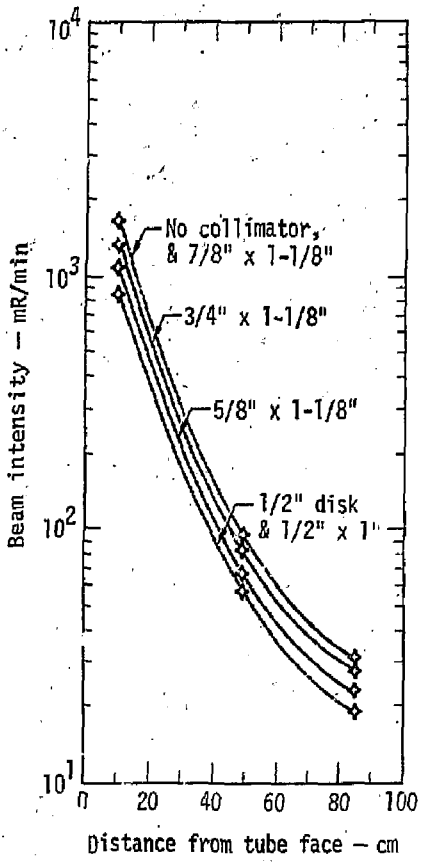

Fig. 20. Intensity versus distance for various collimators. Silver target TRAX (sputtered) 100 μA, 50 kV, no external filter.

scatter cross sections are from 10 to 100 times larger than the Compton cross sections, so little change in spectral distribution is noted. Figure 20 shows this effect for the sputtered target (the foil target was essentially identical) which amounts to nearly a 100% increase in intensity when the bore is changed from 12 to 21 mm (1/2 to 7/8 in.).

Beam purity for the two targets was measured by operating at low power levels and looking down the axis of the beam with a high-resolution 9 mm^2 X 3 mm Si(Li) detector. The resulting spectra were corrected for detector efficiency and compared – they were indistinguishable. Figures 21, 22 and 23 show representative spectra with three typical filter combinations.

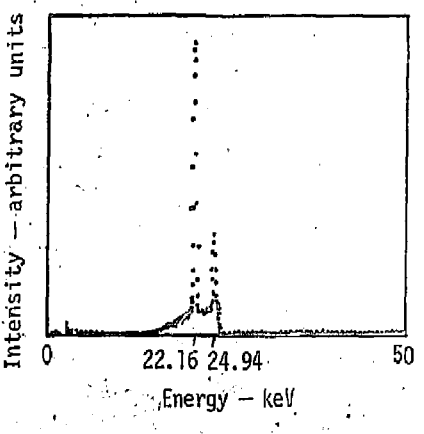

Fig. 21. Output spectrum. Silver target TRAX (sputtered), 50 kV, no filter.

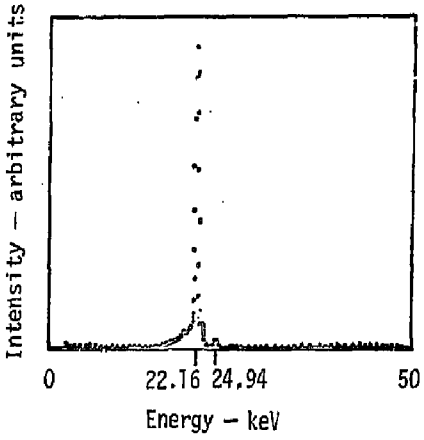

Fig. 22. Output spectrum. Silver target TRAX (sputtered), 50 kV, 0.002-in. Rh filter.

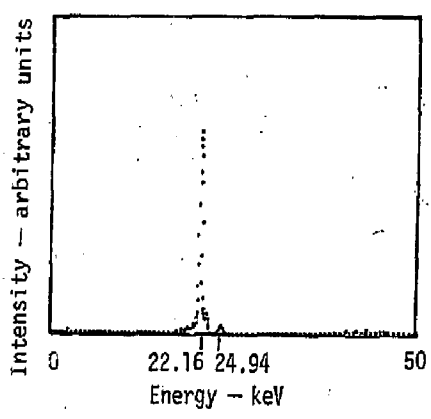

Fig. 23. Output spectrum. Silver target TRAX (sputtered), 50 kV, 0.003-in. Rh + 0.005-in. Ag filter.

Beam uniformity and beam diameter are important parameters for practical use of the tube. A large area of equal illumination permits simultaneous exposure of many TLDs, or a uniform dose to a large detector. To measure these parameters, we exposed sheets of radiographic film to the beam, had the images digitized by a scanning micro-densitometer, and generated contour maps and cross sections which accurately describe beam size and uniformity. Table 7 relates beam diameter to collimator size and distance for both tubes. There was an interesting contrast in beam uniformity between the two tubes. The foil tube showed excellent uniformity and symmetry in the beam. Figures 24 and 25 show a typical contour map and cross section, respectively. The beam is within ±3% in both the horizontal and vertical planes. Figure 26 is the same data presented isometrically. The sputtered tube, however, demonstrates a marked asymmetry in the horizontal plane. Figures 27, 28 and 29 show a contour map and the two cross sections. So far this phenomenon is unexplained, and will probably remain so until the tube is disassembled. One can suspect either misalignment of beam spot and collimator or physical distortion of the converter foil, but proof is yet lacking. Even with this asymmetry, though, the intensity is uniform within about ±10% in the worst cases.*

Finally, we were concerned about outgassing behavior of the sputtered target. Since it is mechanically more complex, more gas-trapping sites exist and we anticipated problems when running at high power. Happily, these problems do not seem to be of practical importance. Operation at 50-W input (the highest sustained levels yet attempted) have shown pressure rises that were within the acceptable range.

On the whole, then, the sputtered target performs in much the same way as the foil target. The slight loss of intensity has little impact upon normal operations and the beam asymmetry, while perplexing, is not gross and will probably be cured in the near future.

Table 7. Beam diameter as a function of collimator size and distance (measured from film)

Distance (cm)	Collimator diameter/length (mm)	Beam diameter (cm)
10	None	9
	12.7	5
	12.7 × 25.4	3.3
	16 × 28.6	3.8
	19.2 × 28.6	4.7
	22.4 × 28.6	5.8
50	None	~40 (off film)
	12.7	18
	12.7 × 25.4	10.5
	16 × 28.6	13
	19.2 × 28.6	16
	22.4 × 28.6	17
85	12.7 × 25.4	18.6

*The tube was later disassembled, and the target was found to have moved roughly 3 mm (due to axial loading on the high-voltage feed-through from the cable connector). This easily accounts for the asymmetry, and will be corrected in future assemblies.

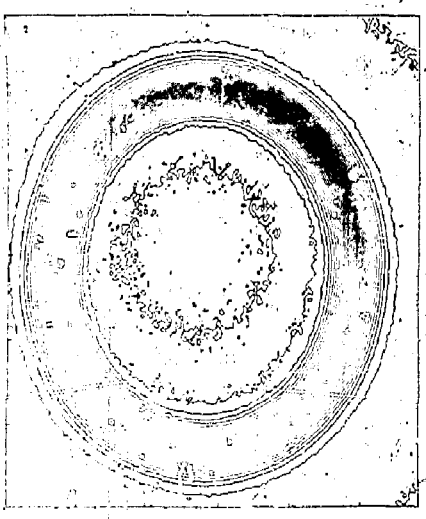

Fig. 24. Contour map of beam intensity – contour lines represent 2.5% intensity change. Silver target TRAX-foil, 50 kV, no filter, 10-cm 0.5- × 1-in. collimator.

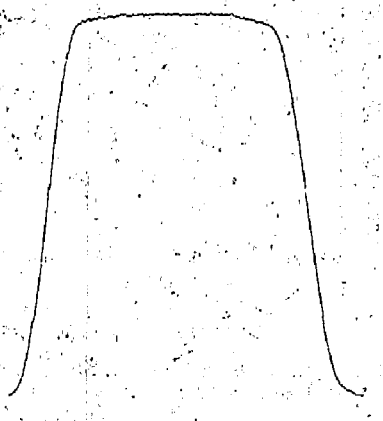

Fig. 25. Horizontal cross section of beam intensity. Silver target TRAX-foil, 50 kV, no filter, 10-cm 0.5- × 1-in. collimator.

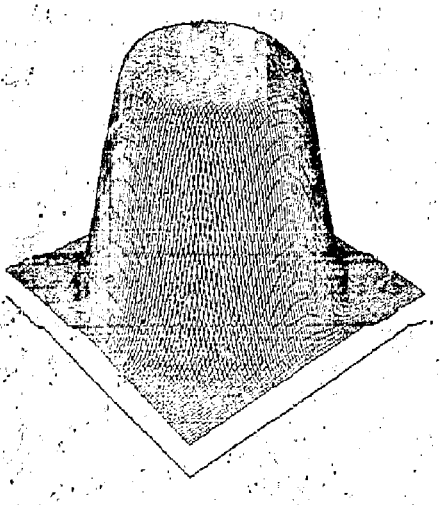

Fig. 26. Isometric presentation of beam intensity. Silver target TRAX-foil, 50 kV, no filter, 10-cm 0.5- × 1-in. collimator.

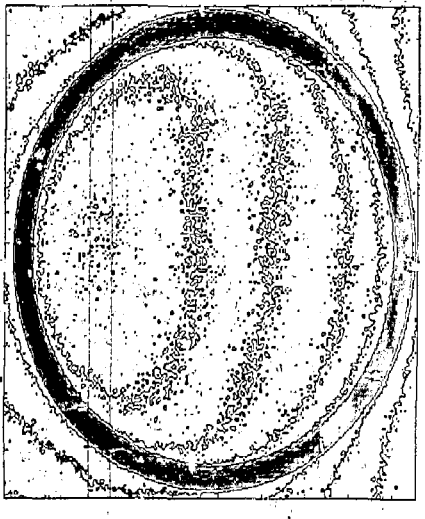

Fig. 27. Contour map of beam intensity. Contour lines represent 3.0% intensity change. Silver target TRAX (sputtered), 50 kV, no filter, 10-cm 0.5- × 1-in. collimator.

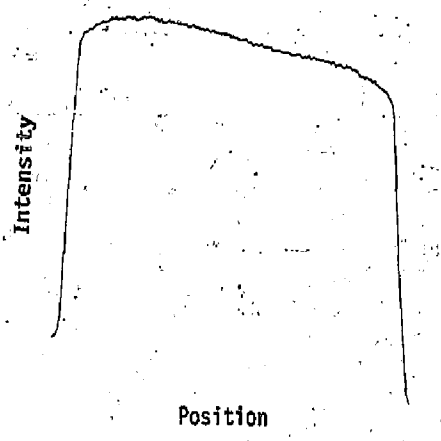

Fig. 28. Horizontal cross section of beam intensity. Silver target TRAX (sputtered), 50 kV, no filter, 10-cm 0.5- x 1-in. collimator.

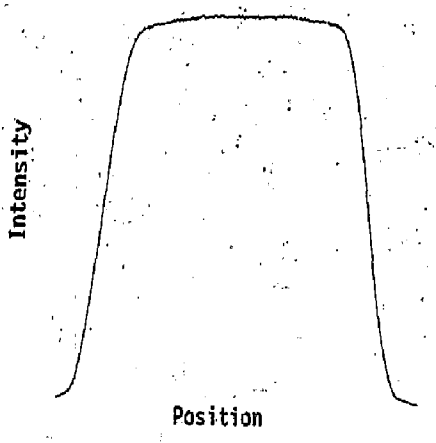

Fig. 29. Vertical cross section of beam intensity. Silver target TRAX (sputtered), 50 kV, no filter, 10-cm 0.5- x 1-in. collimator.

HEPA-Filter Smoke Plugging Tests Using LLL Large Scale Fire Test Facility

Introduction. In our previous report [26] we described the LLL Full-Scale Fire Test Facility, and we summarized some of the tests and results obtained in preliminary experiments conducted to evaluate the smoke plugging of the HEPA filters. Since that time, we have conducted a number of tests on two fuels to characterize the smoke generated by them, and have done a series of screening tests on smoke abatement countermeasures.

Test History. Because we were unable to characterize the smokes from our burns involving *mixed furnishings*, we decided to investigate individual fuels in the form of cross-piled cribs. Furthermore, because some of these materials are of the plastic family which tends to melt and burn away during a test, we decided to use a cage to hold the cross-membered crib.

In Test 1 (and Test 2, a check of Test 1) we used Douglas fir as the fuel in the caged wood crib configuration.

In Tests 3 and 4 we used a fire-retarded polymethylmethacrylate, used frequently in ERDA laboratories for gloved box window materials. In Test 3 the ventilation was the normal rate; i.e., 250 ℓ/s. In Test 4 the ventilation rate was doubled.

Test Series 5, which consisted of 18 sub-tests, employed diesel oil floated in a pan of water as the fuel; the initial ventilation rate was 250 ℓ/s in all cases.

Tests 6, 7 and 8 were conducted using caged Douglas fir (DF) wood cribs to evaluate the more promising scrubbing techniques found in the No. 5 series. The last test, No. 9, was conducted, again using a Douglas fir caged wood crib, to ascertain the effect of a standard sprinkler system.

Results. The essential data from these tests are summarized in Table 8 from which the following observations are made:

- The caging of wood as compared to the previous use of an uncaged cross-piled crib resulted in much faster smoke-particulate generation and consequently a faster filter plugging (in the previous report the standard cross-piled wood crib generated smokes which plugged the filter in about 15 minutes. This contrasts with the 6-minute plugging time observed in Tests 1 and 2).

  The polymethylmethacrylate fuel burned at the normal ventilation rate also caused a fast plugging of the filter, whereas a crib of the same material at a higher ventilation rate did not cause plugging for up to 24 minutes.
- Of the various screening tests (Series 5 using diesel oil fuel) the use of the chevron-type scrubber at full water flow (5.0 ℓ/s) or the two sonic nozzles used in series each at 0.6 ℓ/s seemed to do a reasonable job of smoke particulate scrubbing. These were therefore tried with some variations in Runs 6, 7 and 8.

Table 8. - Large-scale burns

No.	Date	Purpose	Fuel	Vent (ℓ/s)	Remarks
1	7/16/76	Effect of (caged) wood crib *moderate ventilation*	Wood-DF[a] 6.0 kg/m^3 D/C[b] = 0	250 ↓ 160 6.3 min	Fast plugging Smoke: 7.0 g/m^3 9 min Filter soot = 61% tar, 39% C
2	7/28/76	Check of B-1	Wood DF 6.2 kg/m^3	250 ↓ 125 6.1 min	Fast plugging Smoke: 4.6 g/m^3 Filter soot = 56% tar, 44% C
3	8/13/76	*Effect of* FR-PMMA[c] in cage moderate ventilation	FR-PMMA 4.0 kg/m^2 D/C = ∞	250 ↓ 125 8 min	Fast plugging Smoke: 4.1 g/m^3 8 min Filter soot = 67% tar, 33% C 2.6% CO, 4.0% CO_2
4	8/20/76	Effect of well ventilated fire (using unaffected fuel from B-3 on FR-PMMA)	3.33 kg/m^2 D/C = ∞	500 ↓ 250 23.8 min	Slow plugging Smoke: 1.4 g/m^3 8 min No CO, 3.2% CO_2
Series 5	9/10 to 9/14/76	Various countermeasures on diesel smoke	Diesel oil in pan	Initial 250	No HEPA used except for 5.10
5.1	9/10/76	No countermeasures	Diesel oil *in pan*	Initial 250	Chevron scrubber and demister in place
5.2	9/10/76	Repeat of 5.1	Diesel	250	Questionable data
5.3	9/10/76	Use of one sonic spray Plain water	Diesel	250	60% *total removal* 50% of <1 μm part
5.4	9/10/76	Use of one sonic spray 0.1% surfactant	Diesel	250	Samples lost other indications results ~5.3
5.5	9/10/76	Use of Chevron scrubber with own spray 2.0 ℓ/s	Diesel	250	58% total removal 26% <1 μm
5.6	9/14/76	No countermeasures – demister removed	Diesel	250	~4% "dropout" of smoke particle.
5.7	9/14/76	Use of one sonic plain water spray without demister	Diesel	250	~50% smoke particle removal; 60-70% > 2 μm
5.8	9/14/76	Sonic spray 0.1% surf without demirter	Diesel	250	~50% smoke particle removal; ~70% > 3 μm
5.9	9/14/76	Chevron scrubber 2.0 ℓ/s without demister	Diesel	250	~34% overall removal 80% > 3 μm size
5.10	9/14/76	Repeat of 5.9 but with HEPA installed	Diesel	250	No effect on HEPA for 20 min
5.21	9/30/76	Effect of Chevron scrubber 5.0 ℓ/s	Diesel	250	62% particle removal 75% removal > 3 μm
5.22	9/30/76	Chevron scrubber plus sonic spray 0.063 ℓ/s	Diesel	250	~38% particle removal + 50% for <1 μm size
5.23(a)	9/30/76	Sampler #2 oriented upstream	Diesel	250	~32% particle removal for >1 μm size
5.23(b)	9/30/76	Sampler #2 oriented 90% to flow	Diesel	250	~8% particle removal
5.24	9/30/76	Sonicore nozzle using air only	Diesel	250	~26% particle removal
5.25	9/30/76	Two separated Sonicore nozz-water 0.063 ℓ/s each	Diesel	250	~72% particle removal and 1; 37% overall
5.26	9/30/76	Effect of demister only	Diesel	250	Demister slowly clogs. ~23% particle removal – 15 min
5.27	9/30/76	*Effect of* one Sonicore plus demister	Diesel	250	~50% particle removal – demister slowly clogs.

Table 8 (Continued)

No.	Date	Purpose	Fuel	Vent (ℓ/s)	Remarks
6	10/13/76	Effect of two sonic nozzles 0.063 ℓ/s each on caged wood crib smoke (sprays activated at 190 s)	Douglas fir 5.5 kg/m^2	250 ↓ 125 8.3 min	Little improvement in filter life Apparent 65% smoke particulate removal
7	10/22/76	Effect of Chevron scrubber at full flow (5.0 ℓ/s) on caged wood crib smoke	Douglas fir 5.4 kg/m^2	250 ↓ 125 9.8 min	Little improvement in filter life Apparent 60% smoke particulate removal (Check of filter 3 days later shows no plugging)
8	11/1/76	Effect of sonic nozzle and 100-mm demister plus pin type nozzle and 50-mm scrubber	Douglas fir 5.6 kg/m^2	250 ↓ 125 7.4 min	Filter plugged rapidly as in B-6, 7. Smoke concentration ahead of HEPA 1.5 g/m^3 of which 86% < 2 μm
9	12/22/76	Effect of standard sprinkler system on filter life	Douglas fir 5.7 kg/m^2	250 ↓ 230 20.7 min	Sprinklers controlled but did not extinguish the fire. Use of sprinklers prevented filter plugging for duration of test which was terminated at 21 min. Cell overpressurized when sprinklers were operating

[a]Douglas fir.

[b]*Dirty-to-clean fuel ratio.*

[c]Fire-retarded polymethylmethylacrylate.

- The use of these countermeasures on a caged Douglas fir wood crib did not appear to improve filter plugging time significantly.
- A standard sprinkler system activated by the temperature at the sprinkler location controlled the fire but did not extinguish it. However, for the duration of the test (21 minutes) filter plugging appears to have been prevented.
- In most respects Runs 1 and 2 checked each other very well, although they were run two weeks apart.

Discussion. As can be seen from the curves on Fig. 30(a) and (b), representing the pressure drop across the HEPA filter for Burns 6 and 7 respectively, the increase in pressure difference is quite sharp and similar in both tests. This suggests that there is some sudden plugging mechanism occurring in these situations. To try to evaluate this phenomenon, certain observed and calculated data from a number of tests are tabulated on Table 9. Examination of these data suggests that of all the variables examined, the dry bulb temperature of the smoke in the duct at the filter and the absolute humidity at the same location may bear some relationship to filter plugging. Thus, if the dry bulb temperature in the smoke at the filter is well above 100°C, the absolute humidity (grams of water/m^3 of smoke volume) can be high or low. On

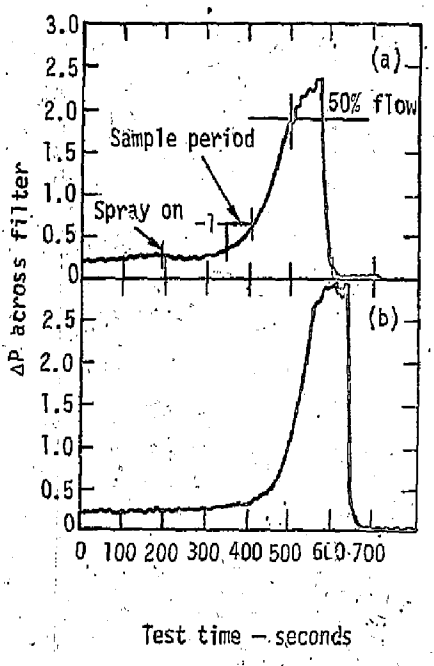

Fig. 30. Pressure drop across HEPA filter. Countermeasure: (a) two sequential sonic nozzles, 0.063-ℓ/s water per nozzle; (b) Chevron scrubber, 5.0-ℓ/s water spray.

Table 9. Critical parameters for HEPA plugging by crib fires

Test No.	Time to peak temp (ks)	Time to plug filter (ks)	Fuel weight loss rate (kg/s)	Filter weight gain (kg)	Absolute humidity of smoke in duct at filter (g(water)/m^3)	Dry bulb temp of smoke in duct at filter (°C)
PB-7[a]	0.37	NO	0.28	0.1	124	185
PB-8	0.24	0.9	0.1	0.9	57	90
PB-8.2	0.34	1.0	0.1	0.9	84	100
B-1	0.16	0.38	0.15	0.1	34	100
B-2	0.16	0.38	0.12	0.1	34	100
B-3	0.52	0.44	0.028	0.2	16	50
B-4[a]	0.7	1.4	0.11	0.43	51	110
B-6	0.17	0.50	0.11	0.13	39	59
B-7	0.15	0.54	0.12	0.65	9	31

[a]Initial ventilation: 500 l/s; for all others, initial ventilation was 250 l/s.

the other hand, if the dry bulb temperature is of the order of 100°C or less, then a low or moderate absolute humidity is accompanied by a fairly fast plugging of the filter.

This suggests that the filter is being plugged either by condensed water or by condensed pyrolysates. In the next few experiments, efforts will be made to attempt to evaluate this point further.

ENHANCED FILTRATION

Introduction

Since the last progress report, we have focused our attention in the following areas:

- Determining filter use rates and exposure conditions
- Modifying the sodium chloride aerosol generation system
- Determining the aerosol charge characteristics
- Studying the effect of screen insulation on filter performance
- Calibrating an active scattering aerosol spectrometer
- Theoretical modelling of filter efficiency, pressure drop and loading capacity characteristics.

Filter Use Rates and Exposure Conditions. High-efficiency particulate air (HEPA) filters are commonly used at radioactive handling facilities to remove airborne contaminants. Filter use rate varies widely with location and operational demands. In 1973, 16,152 filters were used at various nuclear facilities.[27] The current annual use rate is probably greater than 20,000/yr.

Table 10 gives the 1975 usage rates as well as volume and cost data at several facilities. The cost per filter also varies significantly, depending on the specification and overhead requirement. The major cost, however, is not the initial filter expense ($20-$300/filter). The actual cost of materials and labor to buy, change, test and dispose of the filter is often 3 to 10 times the initial cost. Hence a significant savings could be realized if filter service life could be extended.

Table 10. HEPA filter usage in 1975

Facility	Number	Volume (m^3)	Filter cost (K$)
LLL[a]	300	11	41
ORNL[b]	686	65	42
LASL[c]	385	17	15
Rocky Flats[d]	4,000	263	340
Total, 1973	16,000	1,400	2,500
Total, 1975 (est)	20,000	1,800	3,500

[a]J. Lipera, private communication.
[b]W. Porter, private communication.
[c]T. Dofield, private communication.
[d]C. Sheats, private communication.

Since HEPA filters are used in several types of nuclear facilities, it is important to characterize the types of environments in which our polarized electrostatic (dielectrophoretic) prefilters will be used. To date, we have visited filter installations at Lawrence Livermore Laboratory, Los Alamos Scientific Laboratory, Rocky Flats Plant, and Oak Ridge National Laboratory. Perhaps the greatest potential difficulty is attempting to protect the HEPA filters from wet and acid mist conditions. Such hostile environments occur in the Rocky Flats Plant, Building 771, where great amounts of nitric and hydrofluoric acid fumes are generated from the dissolving processes.

Contaminant composition and particle size also varies widely. Table 11 shows size data from several radioactive materials handling facilities. The aerodynamic mass median diameters range from 0.34 to 15.9 μm. Since our sodium chloride test aerosol has a smaller diameter (0.82 μm), the laboratory test represents a more stringent filter test than occurs in the field. The available space for prefilter installation, as one may suspect, also varies considerably. In many gloved box operations, the flex duct could be opened and a prefilter easily installed. If the HEPA filter is housed in a duct, some difficulty may be encountered in placing a prefilter in-line without major duct modification. Relatively thin prefilters would pose no problem for HEPA filter banks in large plenums, but a deep prefilter would seriously inhibit entry into such areas.

Aerosol Generation System. A number of refinements have been added to improve our sodium chloride aerosol generator, and these are shown in Fig. 31.

A humidity controlling system has been added to better stabilize the droplet evaporation rate. The humidity is set to the desired level, and water vapor is added to the air stream by activating a submerged heater. This process is adjusted automatically using a humidity controller.

A 20-litre reservoir has been added as the source of the 1% NaCl solution. Considerable enrichment of salt solution was observed during long (4 hour) runs using 400-ml solution containers.

An active scattering aerosol spectrometer has been added to the system to aid in our particle diagnostics effort. This is also discussed in a subsequent article in this report.

Our filter holder has been completely redesigned, as shown in Figs. 32 and 33. The new system allows us the convenience of loading the screens and filter media outside the plenum and reinserting them, as one integral assembly, into a polyethylene holder. The entire assembly is completely insulated, and an interlock system prevents accidental handling of the electrified screens. This assembly is not only safer, but allows us to experiment with varying filter thicknesses and screen configurations.

Determining Aerosol Charge Characteristics. A charge distribution can be obtained by using an electrostatic precipitator[30] in conjunction with a flame photometer, as shown in Fig. 34.

The precipitator is operated with the precipitation voltage on, but without the corona voltage. In this mode, no additional charges are placed on the aerosol particles as they pass through the precipitator. The particles are removed in the precipitator's collection region according to the charge which they possess after

Table 11. Typical particle distributions encountered in nuclear materials handling facilities

Facility	Process	Aerodynamic mass median diameter (μm)	Geometric std dev. (σ_g)	Range (μm)	Principal constituents
LASL[28]	R & D	1.3	2.2	0.4-8.7	Pu
	R & D	2.3	3.5	0.2-28	Pu
	Fabrication	4.0	1.7	1.4-12	Pu
	Recovery	0.34	5.4	0.01-9.9	Pu
	Fabrication	2.7	2.4	0.5-26	Pu
Rocky Flats[29]	Recovery	0.9[a]	~3	<0.3-13.7	Pu, HF, HNO_3
"Demonstration Plant"[b]	Grinding, 750°C	15.9	1.59	–	Pu, U
"Industrial Plant"[b]	Grinding, 750°C	1.88	1.76	–	Pu, U
"Demonstration, Industrial Plant"[b]	Grinding, 1750°C	2.30	1.65	–	Pu, U
"Industrial Plant"[b]	Grinding, 1750°C	2.09	1.61	–	Pu, U

[a] Count median diameter.

[b] G. Newton, Lovelace Foundation, private communication.

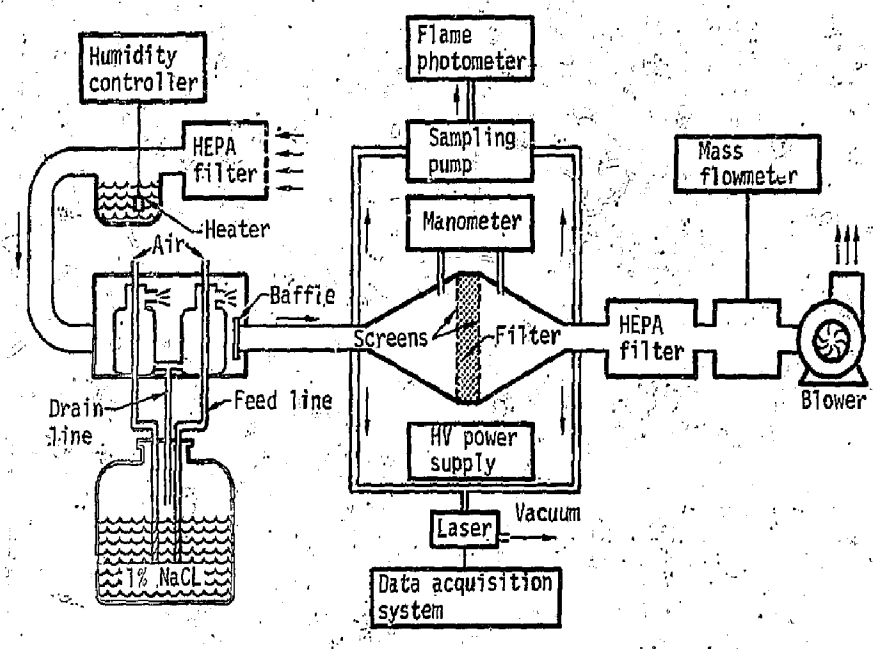

Fig. 31. Schematic diagram of sodium chloride aerosol generation system.

aerosol generation, the flow rate, and the electric field strength. If desired, a ^{85}Kr source can be added to neutralize the aerosol charge.

The drift velocity[31] – that is, the velocity at which the particles move in the precipitator's electric field toward the collection region – is

$$w = E\,Z \qquad (13)$$

where

E = the electric field

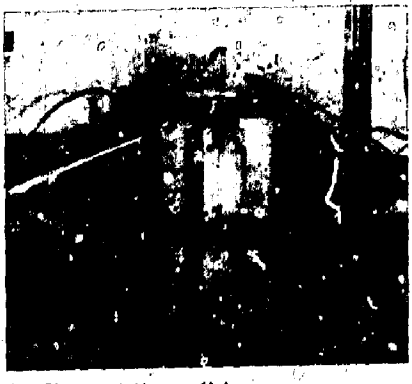

Fig. 32. Filter holder assembled.

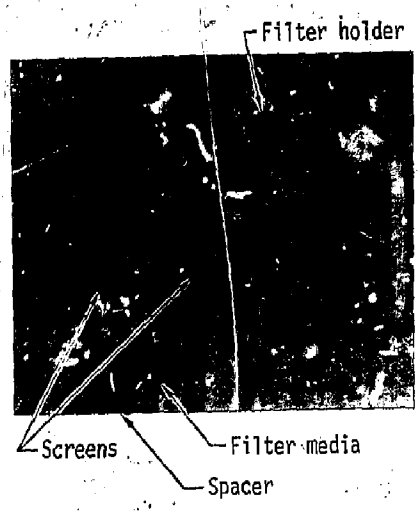

Fig. 33. Filter holder opened.

$Z = \frac{qc}{3\pi\eta d}$ = the electric mobility of the particle

q = number of electron charges on the particle

C = Cunningham slip correction factor

d = particle diameter

η = viscosity of the air.

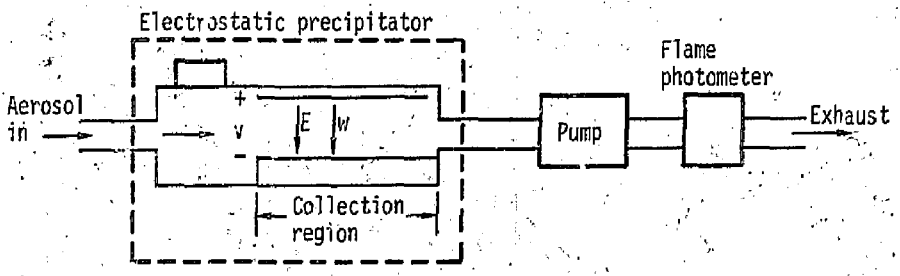

Fig. 34. Charge distribution measurement system.

By comparing the drift velocity with the linear flow velocity, the distance required for precipitation of a particle of diameter d and having charge q can be calculated. If the charge is zero, the drift velocity is zero and the particle would not be collected in the precipitator. Also, at higher flow velocities and lower electric fields, the particle has a greater chance of passing through the precipitator.

Experimentally, the flow rate and precipitation fields were varied from 0.4 to 5 ℓ/min and 0 to 5000 V respectively. The effluent NaCl aerosol was monitored with the flame photometer at the various settings. Since the flame photometer measures the mass of the aerosol particles, we assumed that the particles were monodispersed. A spectrum of charge distributions corresponding to various particle sizes is actually required, however, for rigorous work.

The experiment yielded the cumulative charge distribution curves shown in Fig. 35 for 0.8- and 0.9-μm particles. Eighty percent of the particles comprising the aerosol have one or more charges, and both curves imply that the median charge on a particle is 12 to 14 electron charges.

We can also theoretically predict the average charge on a particle. Mercer[32] gives an empirical equation which predicts the charge given to aerosol particles during the atomization process. The average charge, $\bar{q}$, is

$$\bar{q} = 6\, d_w^{1/2} \qquad (14)$$

where

d_w = droplet particle diameter.

Note that the water droplet before evaporation has a size

$$d_w = \frac{d}{C^{0.333}}$$

where

C = NaCl concentration.

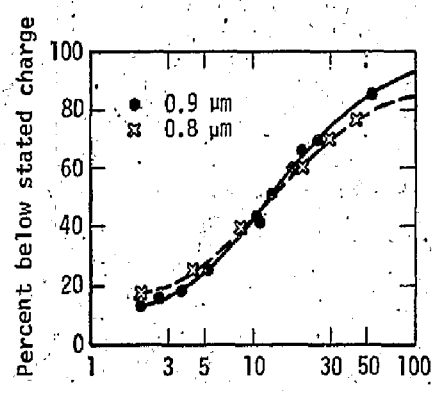

Fig. 35. Cumulative charge distribution curves for 0.8 and 0.9 μm NaCl aerosols.

A 1% solution yield $d_w = 3.7$ for an evaporated drop, d = 0.8 μm. Then $\bar{q} = 6\sqrt{3.7}$ or about 12 charges, which compares favorably with experiment.

Effect of Screen Insulation on Filter Performance. Dielectrophoretic filtration theory currently does not contain any variables which directly relate to screen composition. The bulk of the previous work has been done with uninsulated wires or screens. According to the premises set forth in elementary physics texts, if the screens or wires could be coated with a dielectric, the field around the filtering fibers could be maintained but little or no current would flow even if the filter were collecting purely conductive materials.

Figure 36 shows the results from a series of tests using bare and insulated screens. The insulation was a 10-mil-thick, vacuum-deposited, proprietary material with a dielectric strength of approximately 1 kV/mil. Tests were conducted with the negative high voltage either up- or downstream from the 12.7-mm-thick fiberglass filter media. The other screen was maintained at ground.

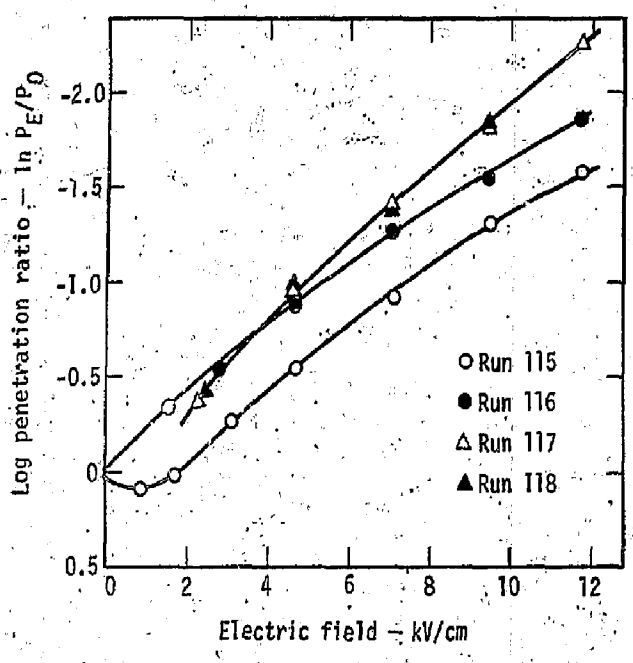

Fig. 36. Penetration ratio as a function of electric field for bare and insulated screens. Run 115 – insulated screen, HV front; Run 116 – insulated screen, HV back; Run 117 – bare screen, HV front; Run 118 – bare screen, HV back.

Figure 36 shows the log of the penetration ratio as a function of the electric field. P_0 is the initial penetration with no voltage applied. Using this *representation*, we can normalize data with different initial efficiencies. The filters with the best efficiency (lowest penetration) characteristics are those represented by the steepest slopes.

Figure 36 reveals some interesting data. The uncoated screens exhibit the same penetration characteristics, regardless of field orientation. The coated screens, however, show two distinct penetration curves, depending on field orientation. With the high voltage on the front plate (i.e., electric field opposing the direction of flow) the penetration decreases as usual as the electric field is increased. At higher electric field, the penetration is somewhat higher than with the uncoated screens. Reversing the screen polarity causes some rather unexpected results. Raising the screen voltage to 1 kV/cm causes the penetration to first *increase* and then decrease as the electric field is further increased.

The reasons for this phenomenon are not clearly understood. The aerosol is in a highly charged condition. Perhaps the charge is neutralized as the particles pass in close proximity of the uncoated screens. In the case of the insulated screens, the particles appear to retain their charge and hence, if the field orientation permits, are actually repelled from the leading edge of the fiber. Increasing the field causes the particles to be attracted and retained on the back side of the fiber. Such a process, however, causes a significant reduction in efficiency. Further investigation of this phenomenon is planned.

Theory of Electric Field on Filter Media

When an electric field is applied across a fibrous filter mat, the fibers and aerosols become polarized. This polarization results in a net attractive force. In addition, if either the fibers or the particles are charged, an enhanced Coulombic effect is also observed. Figure 37 shows the lines of force around a cross section of a single fiber that are due to the two interactions. If the particle trajectory is in the direction of the arrows the force is attractive, while in the opposite direction the force is repulsive. Although the two electric force fields are shown separate in Fig. 37, in reality, they are both combined with the complex hydrodynamic force field to describe the resultant force on an aerosol particle. Such a complete theoretical development has not yet been performed.

The various theoretical treatments of filtration due to either hydrodynamic or electrical forces attempt to obtain an expression for the single fiber efficiency, η. Once η is obtained, the filter efficiency E for a mat of fibers can be determined from the following equation:

$$E = 1 - P = 1 - e^{-\left[\frac{4\alpha x}{\pi D(1-\alpha)}\right]\eta} \qquad (8)$$

where

P is the fraction of particles penetrating through the filter,

α is fiber volume fraction of the filter,

D is the diameter of the fiber in cm, and

X is the filter mat thickness in cm.

We have made an evaluation of the two available theories, one due to Rivers[33] and the other due to Zebel,[34] and have found that the Zebel theory can better represent experimental data. River's theory, described in the last progress report, does not consider any of the hydrodynamic forces, whereas Zebel's theory considers only the particle interception forces and neglects the important inertial and diffusion forces. A key experimental test that distinguishes between the two theories is the secondary effect of filter velocity, v, on the filter efficiency. The primary effect of velocity is inversely proportional to the single fiber efficiency η [see v in Eq. (9) and η in Eq. (8)] and therefore inversely proportional to ln P. Plotting the data as a function of the product v ln P removes the primary effect of velocity and shows the secondary effect, if any, due to velocity. Figure 38 shows that River's theory has no secondary velocity dependence while the Zebel theory shows a definite dependence. Experimentally, the secondary velocity dependence agrees very well qualitatively with the Zebel theory which is therefore used in our initial theoretical investigation.

The equation describing Zebel's theory of filtration in the presence of an electric field is given in Eq. (9). To simplify the expression, we have used the logarithm of the penetration ratio rather than the efficiency.

$$\ln\left(\frac{P_E}{P_0}\right) = -\left[\frac{4\ \alpha X}{\pi D(1-\alpha)}\right]\left[\left(\frac{\epsilon_p - 1}{\epsilon_p + 2}\right)\left(\frac{\epsilon_f - 1}{\epsilon_f + 1}\right)\frac{d^2E^2C}{12\pi\mu Dv} + \frac{neEC}{3\pi\mu dv}\left(\frac{1 + \frac{\epsilon_f - 1}{\epsilon_f + 1}}{1 + \frac{neEC}{3\pi\mu dv}}\right)\right] \qquad (9)$$

where

P_E is the aerosol penetration with an applied electric field,

P_0 is the aerosol penetration without an electric field

ϵ_p is the dielectric constant of the particle

ϵ_f is the dielectric constant of the fiber

d is the diameter of the particle, cm

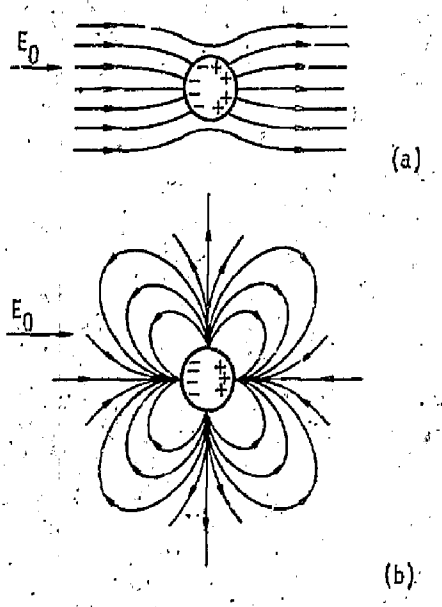

Fig. 37. Lines of force due to applied electric field E_0 for (a) charge and induced dipole interactions (Coulombic), and (b) induced dipole and induced dipole interactions (polarization).

E is the applied electric field, esu

C is the Cunningham slip correction factor

μ is the viscosity of the air, poise

v is the air velocity inside the filter (for our filters v is approximately equal to the filter face velocity V), cm/s

n is the number of elementary charges on a particle

e is a unit of elementary charge, esu

The ratio P_E/P_0 is used to cancel all terms from the equation that do not pertain to the filtration effects of the electric field. Also note that the two terms in the second bracket are equal to the single fiber efficiency due to the electric field. The first of these terms is due to polarization forces and the second is due to Coulombic forces.

This equation was used to systematically investigate the parameters involved in filtration. Figure 39 shows the effect of the electric field and different size particles on $\ln(P_E/P_0)$. The behavior of the graphs in this figure is explained by noting that the polarization contribution is proportional to d^2E^2 while the Coulombic contribution is proportional to E/d. The effect of the other variables on filtration can be found elsewhere.[35]

No quantitative comparison between experiments and Zebel's theory was made because the filter-loading capacity and efficiency measurements were determined

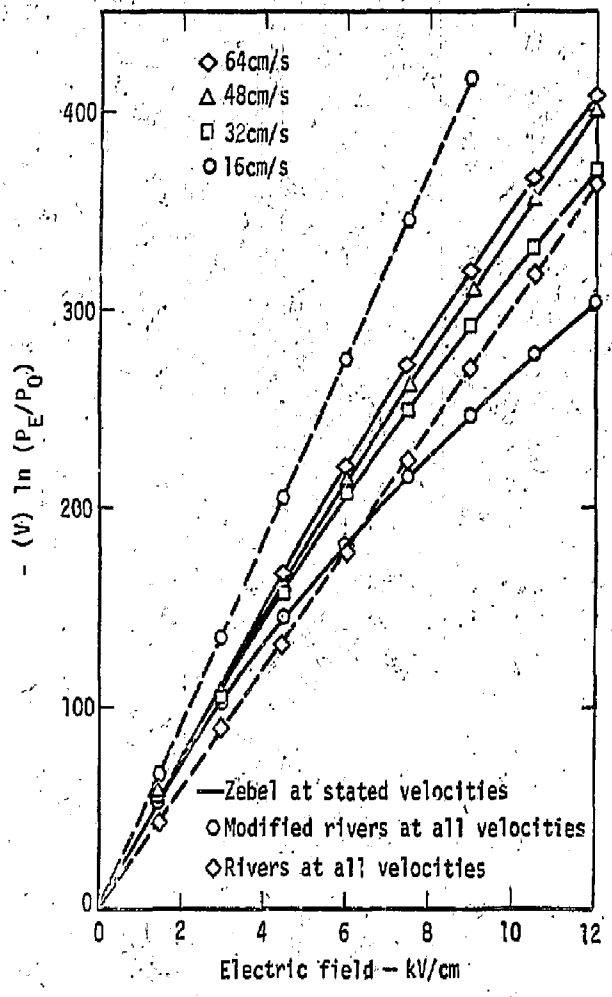

Fig. 38. Theoretical secondary effects of velocity on filter penetration as a function of applied electric field. Dashed curve is River's theory at all velocities. Solid curves represent Zebel's theory at the stated velocities.

as one test. Although this approach was necessary to rapidly screen many filter candidates, the filter efficiency from these tests was erroneously high. Figure 40 shows the significant increase in the filter efficiency that is observed when the concentration of aerosols is increased by four times. Since we now have several promising filter media, the filter-loading and efficiency tests will be conducted as two separate tests.

Even before a quantitative comparison of Zebel's theory is made with a separate efficiency test, it is already apparent that a new theory will have to be developed to explain the experimental data. Figure 41 shows the experimental single fiber efficiency plotted against the applied electric field for three filters having different fiber sizes. The observed trend of increasing efficiency with increasing fiber size is opposite to what would be expected from Zebel's theory or the increasing efficiency due to filter loading. In addition, several effects involving particle charge, the electrode grids, and the electric field described in the July-September Progress Report[35] are also not explained by Zebel's theory.

Although the important effect of particle loading on filter efficiency was widely recognized for many years, no theoretical analysis was made of this phenomenon. We therefore developed a theory,[35] shown by Eq. (10), that describes the increasing efficiency of a filter as it loads up with particles:

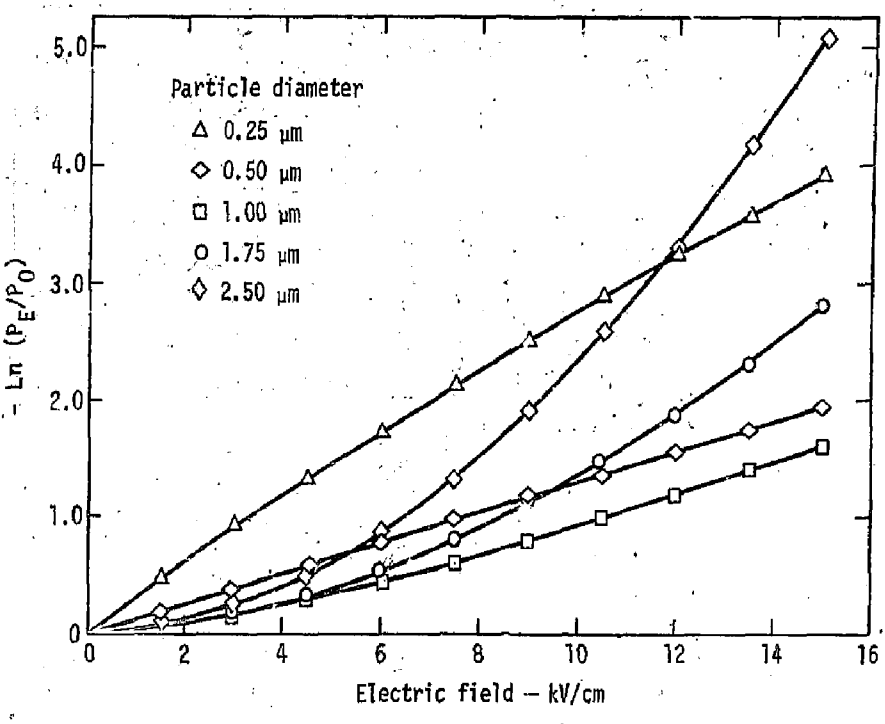

Fig. 39. Theoretical effect of particle size on the logarithm of the filter penetration ratio as a function of applied electric field.

$$N(t) = \frac{N_o e^{-\left[\frac{4\alpha X}{\pi D(1-\alpha)}\eta_F + \frac{\pi V t d^2 N_o}{8}\eta_p\right]}}{1 + \frac{3 M(t)\eta_p}{4 d\rho A}} \quad (10)$$

$$M(t) = \frac{\pi d^3 \rho}{6} A N_o V t \left\{1 - e^{-\left[\frac{4\alpha X}{\pi D(1-\alpha)}\eta_F + \frac{\pi V t d^2 N_o}{8}\eta_p\right]}\right\} \quad (11)$$

where

- $N(t)$ is the number concentration of aerosols penetrating through the filter after time t (cm^{-3}),
- N_o is the number concentration of aerosols upstream of the filter (cm^{-3}),
- η_F is the aerosol collection efficiency for single fibers
- t is the time (s),
- η_p is the aerosol collection efficiency for particles already trapped in the filter,
- ρ is the density of the aerosol particles (g/cm^3),
- A is the face area of the filter (cm^2).

The mass of particles M(t) collected after time t is given by[35]

All other variables were previously defined.

The basic concept of this theory is that the particles once trapped by the filter can trap other particles. This leads to a very large compounding effect as an increasing number of particles are trapped within the filter.

We have also developed a theory to explain the increase in pressure drop as particles load the filter.[35] The theory represented by the equation below makes use of previous pressure-drop theories for unloaded filters.

$$\Delta P(t) = 4\mu V X\left[\frac{\alpha^{3/2}}{D^2} + \frac{[M(t)]^{3/2}}{(\rho A X)^{3/2} d^2}\right] \quad (12)$$

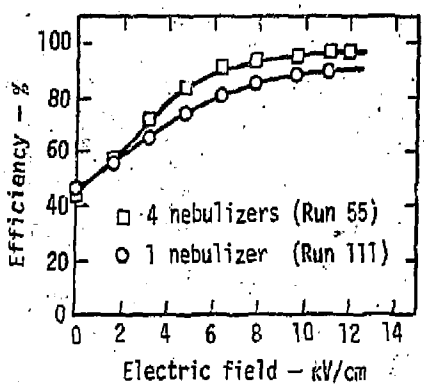

Fig. 40. *Experimental effect of filter loading on efficiency as a function of applied electric field.*

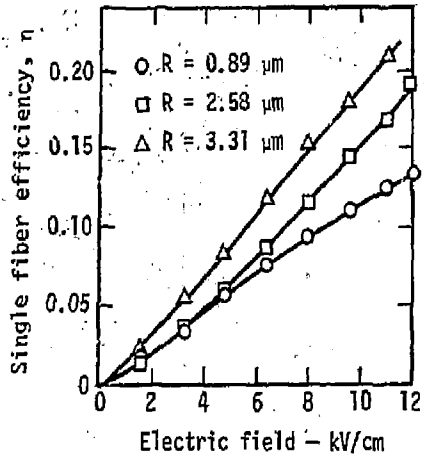

Fig. 41. *Experimental effect of fiber radius on the single-fiber efficiency as a function of applied electric field.* Run 83 – R = 0.89 μm; Run 85 – R = 2.58 μm; Run 87 – R = 3.31 μm.

where

$\Delta P(t)$ is the pressure drop across the filter after time t (Pa).

The other variables have been defined previously.

A quantitative comparison of the experimental increase in filter efficiency and pressure drop will be made with the above theories.

Particle Size Measurement Using Laser Light Scattering

Particle size is important in evaluating the efficiency of the air filters used in the Enhanced Filtration program. Existing theoretical models on dielectrophoresis generated by Zebel and Rivers[33,34] (used in another article within this report) describe the collection efficiency of fibrous air filters as a function of filter characteristics and applied electric field. These models also include variables characteristic of the test aerosol: dielectric constant, particle charge, and particle size. We have now obtained a light-scattering laser spectrometer and data acquisition system (DAS),

Table 12. Sensitivity range of laser spectrometer

Range 0 Channel	(0.60 μm-3.00 μm) size (microns)	Range 1 Channel	(0.35-1.10 μ) size (microns)	Range 2 Channel	(0.20 μ-0.65 μ) size (microns)	Range 3 Channel	(0.15-0.30 μ) size (microns)
1	0.60-0.76	1	0.35-0.40	1	0.20-0.23	1	0.15-0.16
2	0.76-0.92	2	0.40-0.45	2	0.23-0.26	2	0.16-0.17
3	0.92-1.08	3	0.45-0.50	3	0.26-0.29	3	0.17-0.18
4	1.08-1.24	4	0.50-0.55	4	0.29-0.32	4	0.18-0.19
5	1.24-1.40	5	0.55-0.60	5	0.32-0.35	5	0.19-0.20
6	1.40-1.56	6	0.60-0.65	6	0.35-0.38	6	0.20-0.21
7	1.56-1.72	7	0.65-0.70	7	0.38-0.41	7	0.21-0.22
8	1.72-1.88	8	0.70-0.75	8	0.41-0.44	8	0.22-0.23
9	1.88-2.04	9	0.75-0.80	9	0.44-0.47	9	0.23-0.24
0	2.04-2.20	10	0.80-0.85	10	0.47-0.50	10	0.24-0.25
11	2.20-2.36	11	0.85-0.90	11	0.50-0.53	11	0.25-0.26
12	2.36-2.52	12	0.90-0.95	12	0.53-0.56	12	0.26-0.27
13	2.52-2.68	13	0.95-1.00	13	0.56-0.59	13	0.27-0.28
14	2.68-2.84	14	1.00-1.05	14	0.59-0.62	14	0.28-0.29
15	2.84-3.00	15	1.05-1.10	15	0.62-0.65	15	0.29-0.30
0	Total counts	0	Total counts	0	Total counts	0	Total counts

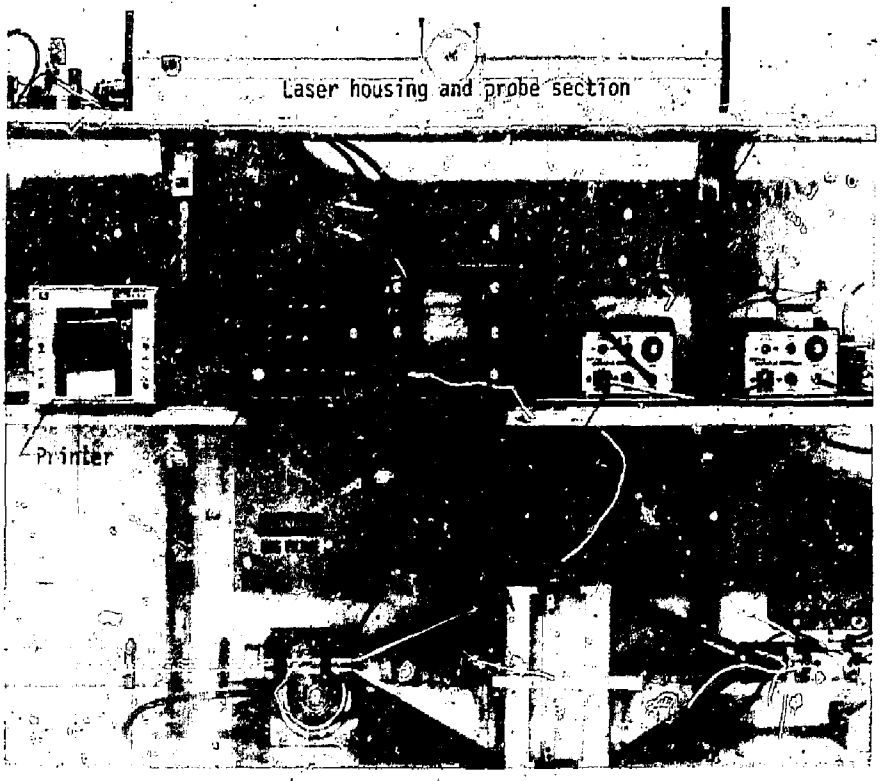

Fig. 42. Particle-measuring systems including laser DAS.

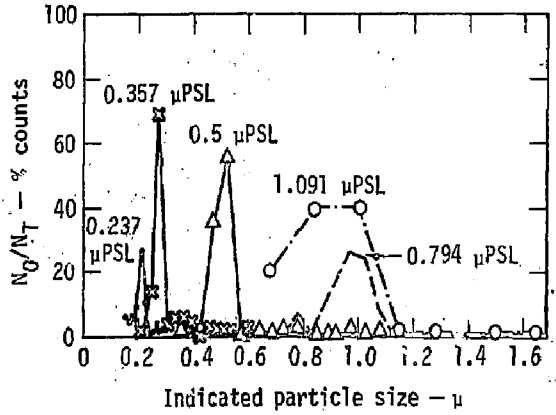

Fig. 43. PSL calibration of laser.

shown in Fig. 42, to measure the particle size distributions.

The spectrometer uses a He-Ne laser (632.8 nm) capable of sizing particles within a range of 0.15-3.00-μm diameter (note Table 12). A stream of particles is passed through the laser beam. For a very dilute aerosol, the particles intersect the laser beam one at a time. The intensity of the light scattered from each particle is measured and the size of the particle is determined by a multi-channel analyzer. Particle size determinations are possible because the intensity of light scattered is proportional to the particle size.

The spectrometer was first calibrated with 0.237-, 0.357-, 0.50-, 0.794- and 1.091-μm-diameter polystyrene latex (PSL) spheres from a Ratec-type nebulizer. Figure 43 illustrates the sizing capability of the laser. This graph shows the observed particle size distribution for the series of monodisperse PSL aerosols having the indicated sizes. The agreement between observed and manufacturer's stated size is

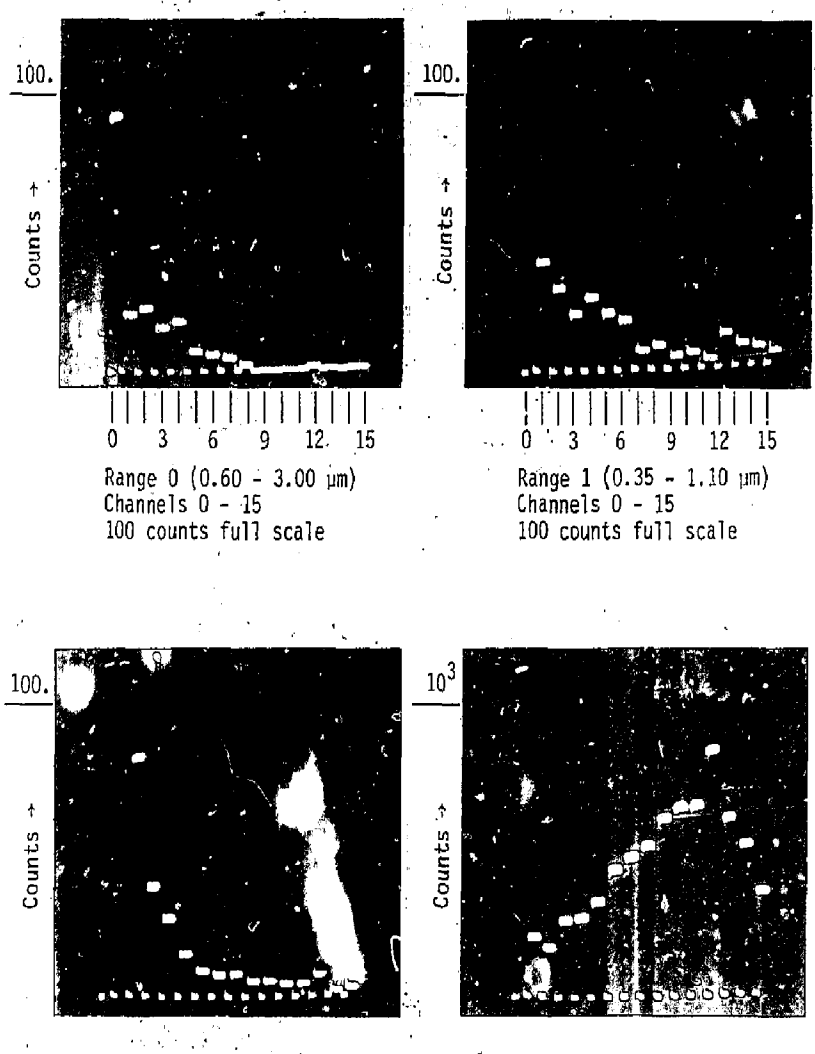

Fig. 44. Histograms of NaCl distribution.

excellent for the 0.237-, 0.357-, and 0.5-μm-diameter PSL spheres. The larger particle sizes appear to be shifted, although the aerosol concentration was not enough to provide adequate size resolution.

We have done some preliminary sizing of our NaCl test aerosol with the laser spectrometer, and these results are summarized in Figs. 44 and 45. Figure 44 shows histograms of the particle size distribution of our test aerosol over each of the four ranges (60 channels) as photographed from the cathode-ray tube display on the data acquisition system. Figure 45 shows a typical range of particle counts for the NaCl aerosol for repeated measurements. Each section refers to one range of the laser spectrometer. Discontinuity in the size spectrum reveals the need for further calibration.

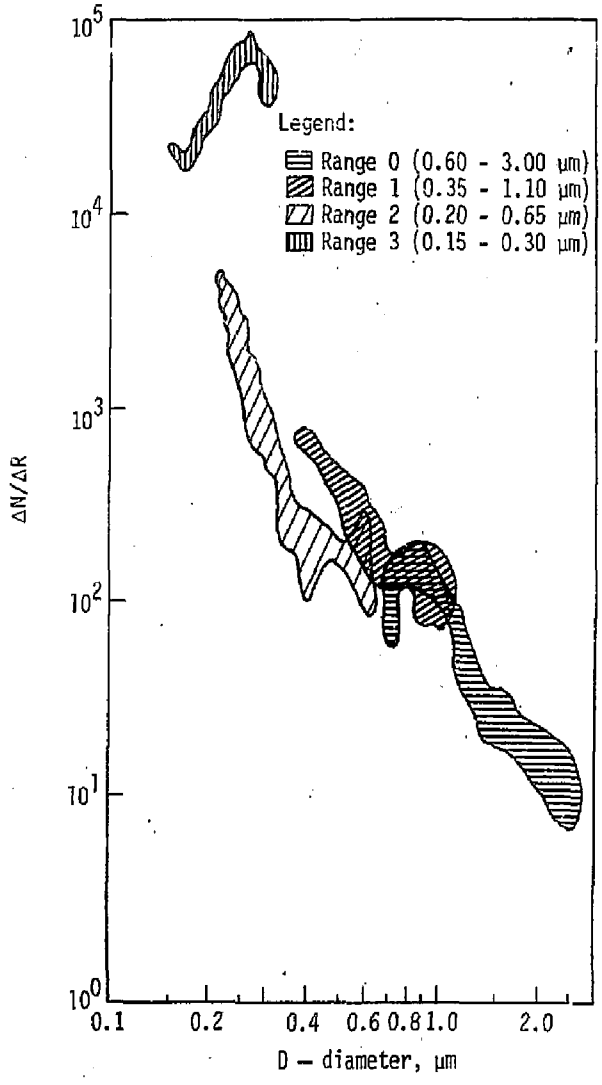

Fig. 45. NaCl aerosol size distribution.

A Method for Determining the Percent Interference in Soil Beryllium Analysis

Each month, the Hazards Control Department's Analytical Laboratory receives 16 environmental air samples to be analyzed for their beryllium content. Airborne soil is collected from permanent air-sampling stations located around the perimeter of LLL and Site 300. These sampling stations contain a high-volume air mover which draws a known volume of air through a 203 X 254-mm filter paper. Airborne soil particulates captured on the filter paper can then be analyzed for their beryllium content.

Since airborne soil can contain many contaminants that may interfere with the analysis for beryllium, a method for determining the percent interference was devised. This method involves the addition of known amounts of beryllium to a sample and measuring the fraction of added beryllium that shows through the interference using an atomic absorption spectrophotometer.

Analytical Method. The air samples are dissolved by digestion on a hot plate using nitric and perchloric acid. The sample is heated to near dryness, then diluted to 25 ml with demineralized water. Two 10-ml aliquots are removed from the flask and spiked with a quantity equal to 0.5 and 1.0 μg beryllium per 25 ml, The remaining 5 ml in the flask is analyzed without addition of beryllium. Three values are obtained for each sample using atomic absorption spectrophotometry:

- 5-ml sample without beryllium added.
- 10-ml sample with 0.5 μg beryllium added.
- 10-ml sample with 1.0 μg beryllium added.

By subtracting the first reading from the second and third we can measure the fraction of the added beryllium to show through any interference. When these values show reasonable agreement, a similar correction can be applied to the first reading.

The following is a calculation of one sample collected during August 1976:

HC #6111

5-ml reading without beryllium addition – 0.45 μg

10-ml reading with 0.5 μg beryllium addition – 0.85 μg

10-ml reading with 1.0 μg beryllium addition – 1.30 μg

Of the 0.5 μg added, 0.85 - 0.45 = 0.40 μg (80%) was recovered. Of the 1.0 μg added, 1.30 - 0.45 = 0.85 μg (85%) was recovered.

The 0.45 μg is corrected for an 80 and 85% recovery to show that an average of 0.55 μg was actually present. Table 13 shows calculations for representative one-month samples.

Conclusion. This method appears to provide a way of correcting analytical results to compensate for interfering contaminants. Further study will determine whether this method is satisfactory or not.

Table 13. Calculations for a representative one-month soil Be analysis

Laboratory number	Readings (μg Be added) 0	0.5	1.0	Corresponding net recovery 0.5	1.0	Average μg Be
6111	0.45	0.85	1.30	0.40 (0.56)[a]	0.85 (0.53)	0.55
6112	0.45	0.80	1.15	0.35 (0.64)	0.70 (0.64)	0.64
6113	0.70	1.05	1.45	0.35 (1.0)	0.75 (0.93)	0.96
6114	0.55	0.90	1.30	0.35 (0.78)	0.75 (0.73)	0.75
6115	0.75	1.1	1.45	0.35 (1.07)	0.70 (1.07)	1.07
6116	0.3	0.7	1.1	0.40 (0.38)	0.80 (0.38)	0.38
6117	0.4	0.8	1.3	0.40 (0.50)	0.90 (0.44)	0.47
6118	0.45	0.85	1.25	0.40 (0.56)	0.80 (0.56)	0.56
6120	0.35	0.70	1.0	0.35 (0.50)	0.65 (0.54)	0.52
6121	0.55	0.85	1.20	0.30 (0.92)	0.65 (0.85)	0.88
6122	0.20	0.55	1.0	0.35 (0.28)	0.80 (0.25)	0.26
6123	0.25	0.70	1.10	0.45 (0.26)	0.85 (0.29)	0.28
6124	0.05	0.5	0.95	0.45 (0.06)	0.90 (0.06)	0.06
6125	1.60	2.00	2.3	0.40 (2.0)	0.70 (2.3)	2.2
6126	0.40	0.85	1.10	0.45 (0.44)	0.70 (0.57)	0.50

[a] Values in parentheses are Be content after recovery correction.

Technical Notes

RADIATION PROTECTION

A Portable Hand and Shoe Counter

A portable hand and shoe counter has been designed for application in emergency field response situations such as Hot Spot. The entire system is housed in a weather-resistant case, shown in Fig. 46. This package provides a means of monitoring personnel hands and shoes without an operator in attendance.

System Description. The system includes a standard camera tripod, a Ludlum count rate meter, two alpha scintillator probes, and an adjustable audible alarm. An adaptor was fabricated to attach one probe head to the top of the tripod to serve as a hand counter. The other probe is mounted in the suitcase as a shoe counter. Figure 47 shows the system set up for use.

Electronics. The Ludlum count rate meter is calibrated for 0-500; 0-5000; 0-50,000; and 0-500,000 counts per minute with a meter response of 3-11 seconds. It is powered by two "D" cells with a battery life of more than 100 hours of continuous use. Figure 48 shows the schematic of the audible alarm system which incorporates an alarm set point of between 200-10,000 counts per minute. The circuitry of the Ludlum instrument was unchanged because the trigger of the alarm system comes from the audio output of the count rate meter. In case of instrument malfunction, an exchange of Ludlum meters can be made with minimum adjustment and down time.

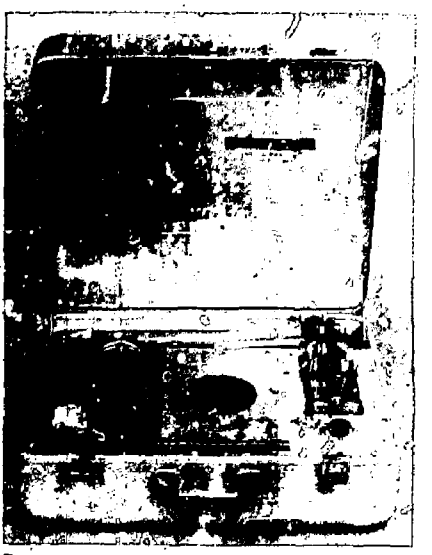

Fig. 46. Portable hand and shoe counter in weather-resistant case.

FORIST, NE 213 Neutron Unfolding Code at LLL

The FERDOR[36] unfolding method is widely used to unfold neutron spectra from pulse-height distributions measured with NE 213 spectrometers. Two spectrum unfolding codes implementing the FERDOR method are currently being distributed by the Radiation Shielding Information Center for the IBM-360. The first code, COOLC,[36] was developed at Oak Ridge National Laboratory. The second code, FORIST,[37-38] is a modified version of COOLC and was developed at the University of Illinois at Urbana-Champaign.

The FORIST code has been received from RSIC, and with minor changes is now operable on the CDC 7600 computers. Changes to the code involved reformatting, tape assignments, and plotting routines.

NUTSPEC, a neutron spectra unfolding code written by Dennis Slaughter, is currently being used at LLL. Results from NUTSPEC will be compared with the more widely accepted FORIST.

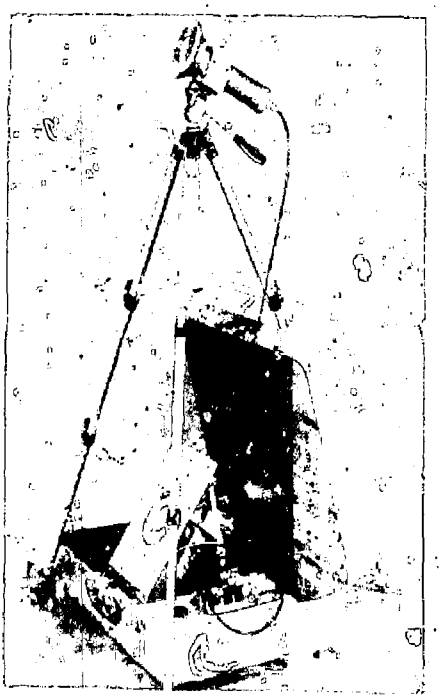

Fig 47. Counting system set up for use.

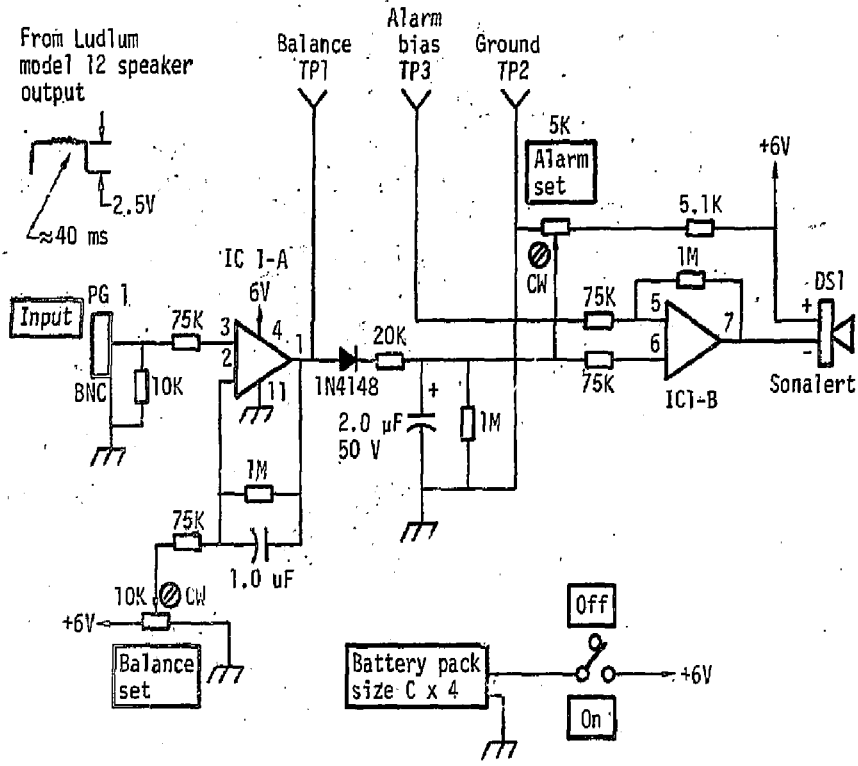

Fig. 48. Schematic of alarm control module.

INDUSTRIAL HYGIENE

Study of LLL Self-Contained Breathing Apparatus Program

The original purpose of this study was to determine the feasibility of using the Metrotech Communications Unit on the Scott 6000 self-contained breathing apparatus (SCBA) in use at LLL. Since the LLL Fire Department is the largest, most frequent user of SCBAs, they were used as the test group for fitting tests with the Metrotech units. However, the study was expanded to take an overall look at the entire SCBA program because the Scott 6000 units currently in use are, by law, to be "grandfathered" out by March 31, 1979, under the approval system of the National Institute for Occupational Safety and Health (NIOSH).

Scope. The use of SCBA, frequency of use, and user groups in the Laboratory were considered during the study. The types and makes of different SCBA units were then examined to see how they would best fit into the program at the Laboratory. Since all of the different makes of SCBAs that were considered in this study had NIOSH approval and thus met minimum operational standards, the main considerations were facepiece fit, ease of maintenance, comfort to the wearer and ease of use, both under emergency conditions and in training.

Table 14 shows the quantitative fitting results of tests performed on LLL firefighters wearing five makes of full-face respirators and a Scott 6000 series mask fitted with a Metrotech communications unit. During the test the firefighters performed six different exercises.

Conclusion. It was concluded that no variance should be requested from ERDA to allow use of the Metrotech communications unit because weight of the unit pulled the facepiece to one side, causing severe leakage around facepiece-to-face seal. Work is now continuing to find a satisfactory way for persons wearing self-contained breathing apparatus to communicate with each other.

Table 14. Quantitative fitting test results

Type of facepiece	Number of firefighters		
	With <1% facepiece leakage	With 1-5% facepiece leakage	With >5% facepiece leakage
MSA Clearvue	28	2	0
MSA Ultravue	28	1	0
Scott 6000 facepiece	18	9	3
Scott 9000 facepiece	9	18	2
Survivair	23	5	1
Scott 6000 facepiece with Metrotech unit	9	16	4

FIRE SAFETY

Measurements of the Combustion Heat Release Rate of Laboratory Construction Materials with a Modified Flame Spread Apparatus

The combustion heat release rate HR^2 from flammable materials has been identified as a sensitive index for comparing and rating the flammable hazards of such materials. Several fire research and testing laboratories have constructed or purchased HR^2 calorimeters for the purpose of either conducting research into the HR^2 properties of a wide variety of combustible materials or for developing a standard test method which can be used to generate criteria for building codes.

The fire research and fire safety sections of the Hazards Control Department had been considering the acquisition of a commercially available HR^2 calorimeter to increase the capability of the Laboratory for assessing the flammable hazards of materials used for the furnishing, finishes and appliances of nuclear laboratories. But there was concern as to the cost effectiveness of this apparatus in terms of the projected needs of the Fire Safety Group. Ideally, the Fire Marshal will determine the fire load of an enclosure or building, and then design a fire protection system suitable to the projected hazard. HR^2 data should be of use in this analysis. However, since there is such a wide variety of enclosure types (laboratories, offices, trailers, shops, computer rooms, libraries, etc.) containing different materials in different configurations, it would be impractical to determine the HR^2 of all these materials. Consequently, the design criteria for fire protection must generally rely on published code information.

In the construction of experimental facilities, test bays, and components (hoods, ducts, hermetically sealed cabinets, electrical and thermal insulations, etc.) the materials of construction may not be covered by standards and codes, so fire protection engineers are not able to estimate their contribution to the total flammable hazard of the enclosures that contain them. Some knowledge of the HR^2 of the more common of these materials would be helpful for fire hazard analysis.

We have modified LLL's radiant-panel surface-flammability apparatus so that it can be used to measure the HR^2 of materials at various flux levels. The E-162 has a provision to measure the heat content of combustion and pyrolysis gases emitted during its normal exposure mode. However, the specimen is oriented such that its top edge is closer to the radiant panel than is the bottom edge. Thus, the radiant flux to the specimen decreases from top to bottom. The modification to convert the E-162 to a simple heat release rate calorimeter consisted of redesigning the specimen support brackets to accept vertical orientation of the specimen at defined distances from the radiant panel. In this way, the heat flux will be uniformly distributed over the surface of the specimen at irradiance levels that depend on its distance from the radiant panel.

Two further alterations to the E-162 were made: (1) the flow capacity of the exhaust duct was increased so that it could accept the total volume of combustion gases and smoke emitted from the specimens, and (2) windshields were installed on the sides, back and top of the apparatus to reduce the effect of spurious draughts on the exposure dynamics.

Figure 49 outlines these changes by showing schematically the essential features of the untouched and modified apparatus. The windshield on the right side of the modified apparatus contains a window so that the time to ignition and burning behavior of the specimen can be recorded on a video system.

To maintain the simplicity of the system, we opted to use the same specimen holders employed for E-162. In E-162, the samples used for surface flame spread

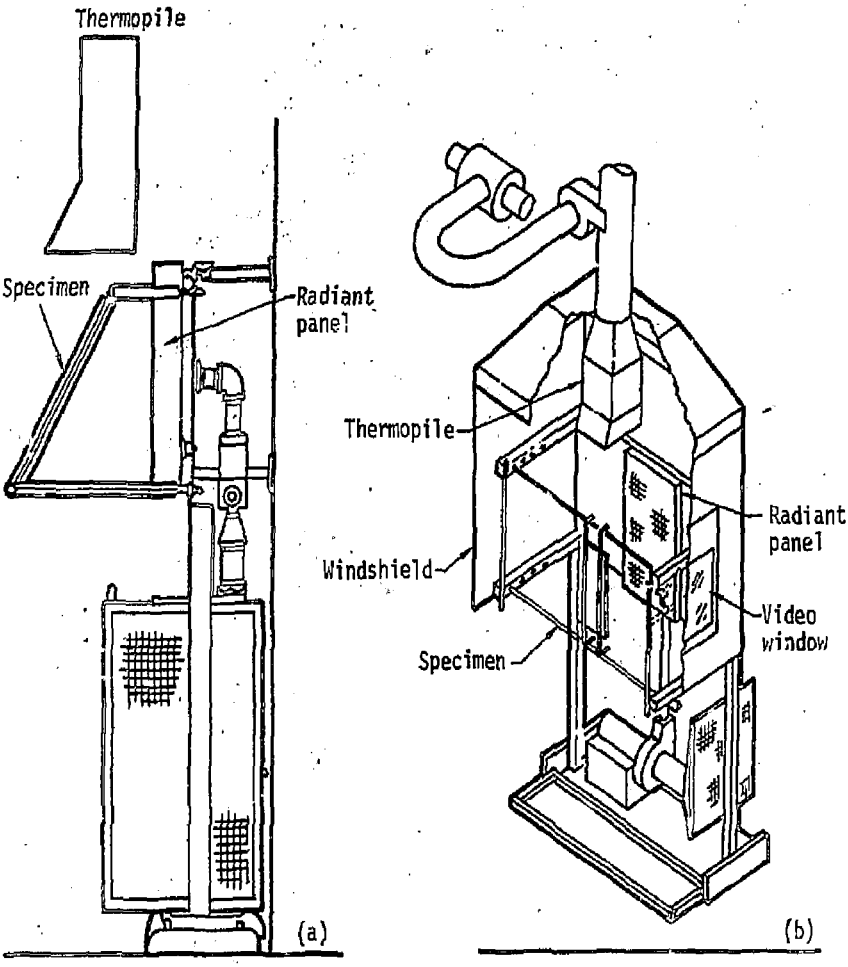

Fig. 49. (a) E-162 apparatus, and (b) modified version.

are 152 mm wide by 457 mm long. In the HR^2 modification, these sample dimensions would overpower the capabilities of the heat-sensing elements to discriminate between the HR^2 of different materials. Thus, simple tests were made to assess the optimum size range for optional testing. These were found to be as follows:

457 mm length for cellulosic films on inert substraits,

152 mm length for unmodified cellulosic materials,

76 mm length for most flammable plastics.

All test materials were conditioned as specified in the ASTM E-162 test method. No other sample pre-preparation methods were instituted, such as sealing the edges and back of the tested specimens.

Figure 50 is a block diagram showing the spatial relationship of the essential components and the diagnostic equipment. A typical exposure involves the following sequence:

- The radiant panel is stabilized such that the radiometer reads 2.35 mV ± 0.04. (This is specified in the E-162 test method as a panel color temperature equivalent to a black-body radiating at 670°C, where the radiometer is located at 1.2 m from the radiant panel.)
- A specimen holder containing a transite board test blank is located at one of the calibrated test

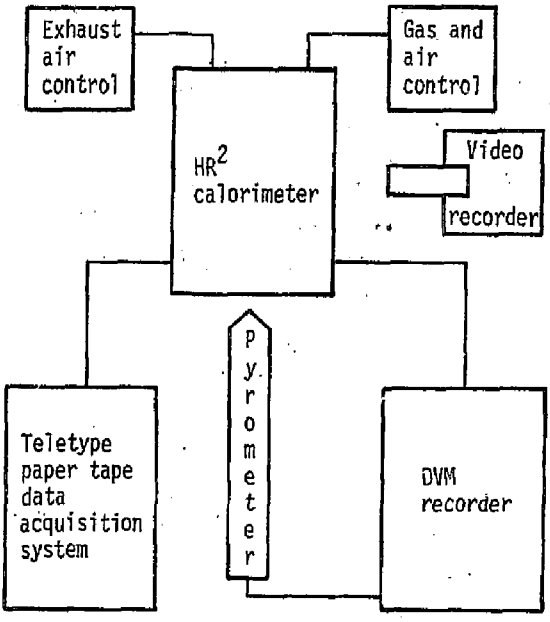

Fig. 50. Spatial relationship of essential components.

positions until a constant output from the exhaust duct thermopile is achieved. During this period the pilot flame is positioned so that it will intercept the gases pyrolyzed from a test sample at a position approximately 25 mm above its top edge.

- When the thermopile indicates a stable EMF, the recorders and video system are started and a sample holder containing a test specimen is installed in place of the test blank. The test specimen area has been sized to insure that flames occurring during the exposure do not reach the thermopile.
- The exposure is terminated when the specimen has apparently been entirely consumed, when the surface distorts toward the radiant panel, or when the material shrinks such that the edges or back surface become involved in combustion.

The output from the thermopile and radiometer are sensed by a digital voltmeter and recorded by a strip chart recorder and a paper tape system. The information on the paper tape is transferred to magnetic tape, and the data are reduced and plotted using a PDP 11 computer.

Because of the simplicity of test specimen preparation and exposure mounting and because of our termination criteria, the exposure duration was relatively short for all but extremely durable materials. The maximum exposure time for wood samples that we were comfortable with was of the order of 200 seconds, so we specified a 3-minute exposure as the standard test duration. The recorded data were:

- The time to ignition t_i
- The time to peak heat release rate t_p
- The peak heat release rate P
- The integrated first minute heat release rate Q_1
- The integrated first 3-minute heat release rate Q_3

The total radiant energy available at the surface of the material (H_t) was calculated as the product of the time to ignition and the panel irradiance (H), and is used as an index of the ignitibility of the tested material.

Table 15 summarizes the data taken during this test series. The materials used were of two categories: those already preconditioned for E-162 tests, and those used in other LLL fire test programs. The column headings are defined above. The tested materials and their predominant gross characteristics are listed in Table 16.

Figures 51(a) through 51(d) are bar graphs that represent the P, Q_1, and Q_3 data contained in Table 15 at input irradiance of H = 5.1, 4.3, 3.5 and 2.6 W/cm^2 respectively. The only materials that show data at all four irradiance levels are: fire-retarded PMMA, Benelex, fiber-reinforce; polyester, white pine, and gypsum board. The Lexan and PVC would not

Table 15. Heat release rate parameters

Material	Input irradiance (H) (W/cm^2)	Time to ignition (t_i) (s)	Time to peak heat release rate (t_p) (s)	Total energy during t_i (H_t) (W)	Peak heat release rate (P) (W/cm^2)	First minute integrated heat release rate (Q_1) (W/cm^2)	3 minute integrated heat release rate (Q_3) (W/cm^2)
Sheet rock	5.1	36.3	24	185	5.45	3.9	–
	4.3	65	25	280	5.0	3.0	–
	3.5	126	22	441	4.1	2.4	–
	2.6	244	58	634	1.9	2.4	–
White pine	5.1	14	34	71	9.2	8.5	8.8
	4.3	33	37	142	12.6	9.3	9.0
	3.5	70	44	244	9.1	8.1	4.8
	2.6	139	47	360	10.2	8.4	5.0
Benelex	5.1	63	108	321	30.1	16.5	26.9
	4.3	136	114	585	34.3	24.2	29.4
	3.5	237	110	830	21.7	13.6	16.9
	2.6	384	80	998	28.0	23.7	24.6
Fiber-reinforced polyester	5.1	115	37	582	12.3	10.4	12.0
	4.3	221	25	949	15.5	13.2	13.2
	3.5	357	25	1250	10.5	11.3	9.1
	2.6	583	43	1516	14.5	10.5	12.0
PMMA (fire-retarded)	5.1	74	216	375	55.2	23.2	36.2
	4.3	111	226	477	54.8	13.9	30.4
	3.5	250	228	875	40.7	9.6	21.5
	2.6	512	280	1331	36.8	14.3	20.4
Polyvinyl chloride	5.1	28[a]	189	142	7.8	3.2	6.4
Lexan (polycarbonate)	5.1	146	103	742	34.2	16.1	28.1
Plastic-coated plywood panelling	4.3	40	63	172	13.2	9.4	8.4
Plastic-covered particle board	4.3	58	106	249	19.6	13.7	13.7
Acoustic ceiling tile	4.3	24	54	103	7.5	5.8	4.8

[a]Ignition of pyrolized gas at pilot flame only.

Table 16. Predominant characteristics of tested materials

Material	Color	Exposed area (cm^2)	Thickness (cm)	Weight (g)	Density (g/cm^2)
Gypsum board	White	580	0.05	64[b]	0.544
Pine wood	White	201	0.693	76.8	0.552
Benelex	Dark brown	100	0.909	147.0	1.62
Polyvinyl chloride (PVC)	Navy gray	100	1.20	198.1	1.65
Fiber-reinforced polyester (FRP)	Light brown	100	0.911	218.1	2.40
Lexan (polycarbonate)	Window clear	100	0.929	127.1	1.37
PMMA (fire-retarded)	Window clear	100	0.852	123.0	1.49
Acoustical tile	White	201	1.77	136.9	0.384
Plastic-coated plywood	Dark wood grain	201	0.373	44.6	0.594
Plastic-coated particle board	Light wood grain	201	0.980	146.7	0.744

[b]To obtain weight of surface paper contributing to the heat release rate, the gypsum board specimen was weighed, then the front surface paper was burned off and the specimen reweighed; the difference is the listed weight.

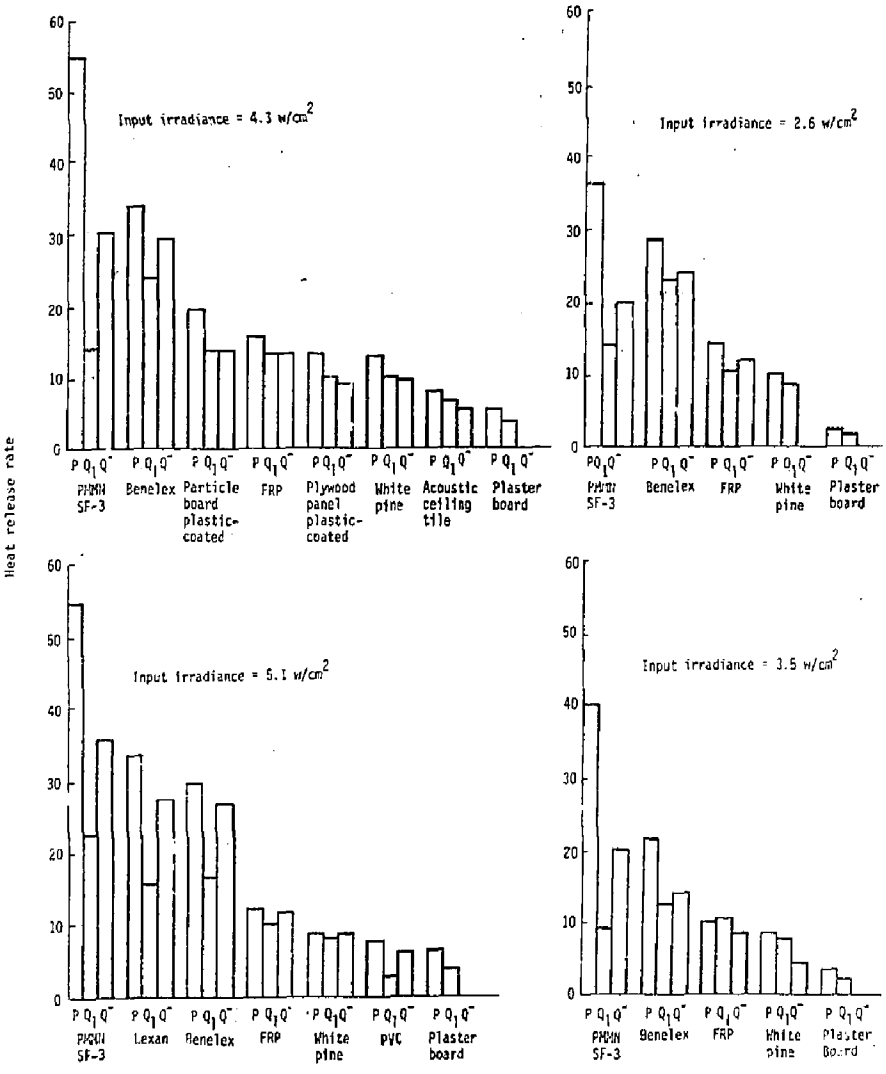

Fig. 51. Bar graphs representing heat release rates for different materials.

ignite below H = 5.1 W/cm^2, and we had only a limited supply of the composite building materials (i.e., the plastic-coated plywood and fiberboard and acoustic tile), so we exposed those samples to an intermediate irradiance level.

In all cases, the fire-retarded PMMA exhibited a larger P value than any of the other tested materials. However, the 1- and 3-minute integrated values are comparable to or less than Benelex and fire-retarded polyester at H $\leq$ 4.3 W/cm^2. This is deceiving since in all exposures, the peak HR^2 for the PMMA was not attained until sometime after 3 minutes, thus the Q_3 value did not include the period of highest heat release rate of the exposure. Furthermore, we note from Table 15 that the time to ignition and the total heat absorbed during this period are relatively high over the exposure schedule. So, while this material may exhibit high HR^2 values, it is a slow starter.

White pine exhibits the shortest time to ignition and moderately low P, Q_1, and Q_3 values. Thus, the total

hazard of this or similar cellulosic materials is not insignificant because of their relative ease of ignition. The lowest release rate data were obtained with the plaster board. In fact, it was not possible to obtain Q_3 values because the total burning duration was of the order of 1 minute.

A final report is in preparation pending further analysis of the data, and a presentation is scheduled at the University of San Francisco late in January 1977. If further research is continued with this apparatus, it will involve the heat release rate of horizontal pools of burning liquid fuels and plastics. Otherwise, the apparatus will be used only as a survey device in support of the Fire Safety Section of Hazards Control.

Flammable Hazards of Christmas Trees on Display

Introduction. The growing interest in general fire safety at LLL has expanded the use of the Fire Test Facility. A current request was concerned with potential hazards of Christmas trees displayed in various Laboratory buildings over the Christmas holidays. To assess this hazard, we conducted simple tests on three excess trees during the week between Christmas and New Years.

Description of Test. We tested a tree that had been allowed to dry out, along with two trees that were properly kept in water-filled bases.

Each tree was installed in the fire test cell and ignited at the base by using 50 ml of isopropyl alcohol in small ceramic dish. Temperature and thermal radiation measurements were taken by using a thermocouple located at the top of the tree and a radiometer with a 90° viewing angle located 3 m away and directed to the center of the tree.

We used time lapse movies and video tapes to record the rate and extent of burning. We weighed the tree before and after the burn.

Summary of Test and Results. The data recorded from each test show the difference in the burning dynamics between a dry tree and a tree that had been kept in water after being cut. Figure 52 compares the temperature rise and duration of the fire from a wet and a dry tree. The difference in the magnitude and duration of the temperature pulse is related to the tree dryness.

The graph of the output of the radiometers (Fig. 53) shows the radiant heat released by the same two trees.

The weight loss by the dry tree was 12 pounds, and at approximately 10,000 BTU/pound this would be 120,000 BTU of radiant energy released. The wet tree lost 4 pounds, equivalent to about 40,000 BTU of radiant energy released.

These data show the potential hazards of a dry Christmas tree in any environment.

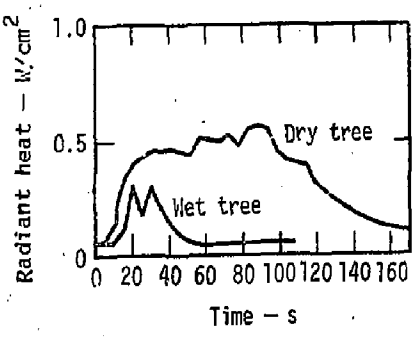

Fig. 52. Temperature rise and fire duration from a wet and a dry tree.

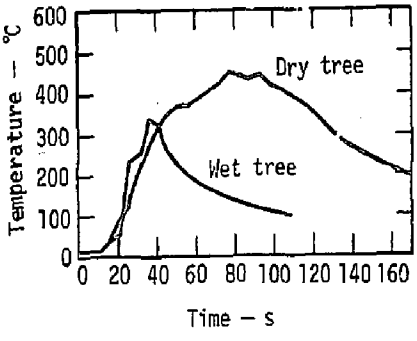

Fig. 53. Radiant heat released by a wet and a dry tree.

Publications

B. J. Held, *A Compliance Respirator Program for the Mining Industry, Present and Future*, Lawrence Livermore Laboratory, Rept. UCRL-78725 (presented at the National Safety Congress, Chicago, Illinois, October 19, 1976, and submitted for publication in the National Safety News)

Until a year ago, the requirements for a respirator program for the mining industry have been almost nonexistent as compared to those industries that are regulated by the Occupational Safety and Health Administration (OSHA). However, the Mining Enforcement and Safety Administration (MESA) made some major changes to Title 30 Code of Federal Regulation, Part 57.5-5, concerning respiratory protection for metal and nonmetal mines, and is proposing similar changes to Parts 70 and 75 for coal mines.

The first of the changes involves respiratory protective equipment requirements; namely, no longer permitting the use of Bureau of Mines approved equipment based on a "grandfathering out" of such devices. Instead, only equipment approved jointly by the National Institute for Occupational Safety and Health (NIOSH) and MESA will be acceptable for use.

The second and most important change is the regulation that a company using any type of respiratory protective devices must have a respiratory program that follows the requirements set forth in the American National Standards Institute Z88.2, "Practices for Respiratory Protection."

Yen Mee Kwok, *Determination of Cyanide in Sewage Water with a Specific Ion Electrode*, Lawrence Livermore Laboratory, Rept. UCRL-77991 (submitted to Analytical Chemistry).

A specific ion electrode method for determining total cyanide in wastewater samples is presented. The standard procedure of heating the sample with EDTA did not give satisfactory results and modifications of the technique were adopted. The interferences of metal ions normally found in sewage water and the formation of EDTA complexes with metal ions were studied. The effect of heating the sample was determined. The stability of free cyanide in an untreated, neutral-to-basic solution was also investigated.

B. J. Held, J. Cross, K. P. Ellis, C. P. Richards and R. Rodrigues, *Evaluation of One-Year Results of the Full-Face Respirator Quantitative Man-Test Fitting Program at Lawrence Livermore Laboratory*, Lawrence Livermore Laboratory, Rept. UCRL-52187 (1976).

In August 1975, Lawrence Livermore Laboratory began to quantitatively fit all employees who are or may be required to wear any type of full-face respirator. After one year, 306 employees have been fitted. A total of 1362 tests were made, using seven makes of full-face respirators. Of the 306 employees fitted, 284 were tested using more than one make of full-face mask.

All employees fitted could get a maximum use limit (MUL)* of at least 100, 8% had a MUL of 100 to 499 on at least one of the makes of masks tested, 11% had a MUL of 500 to 999, 13% had a MUL of 1000 to 1999, 24% had a MUL of 2000 to 4999, and 44% had a MUL greater than 5000. These numbers were derived using the average of the peak leakages occurring during each of six exercises performed while wearing each mask. If the overall average leakage occurring during the six exercises rather than the peak average is used in the calculations, 90% of the employees could obtain a MUL over 1000 on at least one make of mask.

G. O. Nelson, C. P. Richards, R. D. Taylor, A. H. Biermann and H. H. Miller, *Enhanced Filtration: January-March 1976 Progress Report*, Lawrence Livermore Laboratory, Rept. UCID-16949-76-1 (1976).

Twelve types of filter media were placed in an electric field and their efficiency was tested using a sodium chloride aerosol (aerodynamic mass-median diameter was 0.82 micron with a geometric standard deviation of 1.91). Fibrous glass and polypropylene materials show the best overall efficiency and pressure-drop characteristics.

G. O. Nelson, C. P. Richards, R. D. Taylor, A. H. Bierman and H. H. Miller, *Enhanced Filtration: April-June 1976 Progress Report*, Lawrence Livermore Laboratory, Rept. UCID-16949-76-2.

Dielectrophoretic filtration experiments were conducted on glass, polyester, dacron, teflon, wool, acrylic, and polypropylene filter media. A polydispersed (σg = 2.0, ammd = 0.97 μm) sodium chloride particle was used as a test aerosol. All materials exhibited significant increases in efficiency

*The MUL for a respirator is a number which is the multiple of the permissible TWA or excursion limit for toxic materials or the MPC_A for radioactive materials and is obtained by dividing 100 by the percentage facepiece leakage $\left(\text{MUL} = \frac{100}{\% \text{ Leakage}}\right)$

with increasing field strengths. Efficiencies of >99% could be obtained from glass fiber mats using a 13-kV/cm electric field at 16.3-cm/s face velocity.

C. L. Graham, *Accelerator Safety Program at Lawrence Livermore Laboratory*, Lawrence Livermore Laboratory, Rept. UCRL-78600 (presented at the Fourth Conference on Application of Small Accelerators, North Texas State University, Denton, Texas, October 25-27, 1976).

Topics discussed concerning the accelerator safety program at the Lawrence Livermore Laboratory include the design criteria of accelerator shielding, the use of physical barriers, interlocked safety systems, and remote area radiation monitors. Personnel dosimetry requirements, administrative controls for accelerator start-up procedures, reentry procedures, and general operating procedures are also discussed. Examples of the radiation alarm and radiation safety systems for specific accelerator facilities are also given.

J. H. White and C. W. Sundbeck, *Estimates of Cosmic Radiation Using TLD Measurements*, Lawrence Livermore Laboratory, Rept. UCRL-78423 (1976).

In analyzing CaF_2:Dy (TLD-200) data from the environmental monitoring program at the Lawrence Livermore Laboratory, a quantity of significance is the dose to the thermoluminescence dosimeters during shielded storage. This paper describes a method for determining this shield dose, which can then be related to the dose from cosmic radiation. Data, based on quarterly TLD exposure periods, show a range of 43-56 μrads per day in a 75 mm thick lead shield. Observed variations in the shield dose have led to studies of prolonged exposure of TLDs to elevated and reduced temperatures typical of those in the Livermore Valley.

A. J. Toy, Thomas Boegel, and J. J. Cohen, *An Objective Function for the Environmental Assessment of Waste Management Systems*, Lawrence Livermore Laboratory, Rept. UCRL-78727 (presented at The Waste Management 1976 Conference, Tucson, Arizona, October 1976).

Various methods are discussed by which one might judge the impact of radioactive waste management systems. The most significant impact is radiation dose to man. Existing ways of assessing radiation dose significance during normal and accident sequences are discussed. We have postulated that a new way to measure radiation dose significance for the nuclear fuel cycle is to calculate population dose per unit of electricity generated. We also offer some evidence which indicates the radioactive waste management program can be accomplished using, as a limit, 0.1 man-rem/megawatt (electrical)-year.

C. T. Prevo, *Use of the Borrmann Effect to Produce Nearly Monoenergetic X Rays*, Lawrence Livermore Laboratory, Rept. UCRL-78252 (1976).

The use of the Borrmann effect to produce nearly monoenergetic x rays is described. Both theoretical and experimental results are presented for the energy range from 15 to 55 keV. Peak shape, full-widths at half-maximum, and intensities are discussed. In addition, a brief description of a computer code for calculating the theoretical results is given.

References

1. *Hazards Control Progress Report No. 50*, Lawrence Livermore Laboratory, Rept. UCRL-50007-75-1 (1975), p. 5.
2. *Hazards Control Progress Report No. 51*, Lawrence Livermore Laboratory, Rept. UCRL-50007-75-2 (1976), p. 3.
3. *Hazards Control Progress Report No. 52*, Lawrence Livermore Laboratory, Rept. UCRL-50007-76-1 (1976), p. 1.
4. W. J. O'Connell, *A Computer Program for Unfolding Detector Response Effects from a Continuous Gamma Ray Spectrum*, Lawrence Livermore Laboratory, Rept. UCID-30079 (1973).
5. J. F. Mollenauer, *A Computer Analysis for Complex Sodium Iodide Gamma Spectra*, Lawrence Livermore Laboratory, Rept. UCRL-9748 (1961).
6. H. M. Colbert, *SANDYL, A Computer Program for Calculating Combined Photon-Electron Transport in Complex Systems*, Sandia Laboratories, Livermore, Rept. SLL-74-0012 (1974).
7. M. J. Berger and S. M. Seltzer, *Nucl. Instr. Meth.* 104, 317 (1972).
8. Robert E. Strout III, "FORIST, NE 213 Neutron Unfolding Code at LLL," *Hazards Control Progress Report No. 53*, p. 39.
9. W. F. Miller and W. J. Snow, *Rev. Sci. Instr.* **31**, 39 (1960).
10. M. Giannini, P. R. Oliva and M. C. Ramorino, *Nucl. Instr. Meth.* 81, 104 (1970).
11. R. L. Heath, *Scintillation Spectrometry*, 2nd Ed., Vol. 1, IDO-16880-1 (1964).
12. *Hazards Control Progress Report No. 50*, Lawrence Livermore Laboratory, Rept. UCRL-50007-75-2 (1975), p. I.
13. *Hazards Control Progress Report No. 52*, Lawrence Livermore Laboratory, Rept. UCRL-50007-76-1 (1976), p. 40.
14. R. V. Griffith, "Personnel Monitoring Measurements," Symp. Measurements for the Safe Use of Radiation, National Bureau of Standards, Gaithersburg, Md., March 1-4, 1976 (in press).
15. G. M. Hassib, J. W. N. Tuyn and J. DuTrannois, "On the Electrochemical Etching of Neutron-Induced Tracks in Plastics and Its Application to Personnel Neutron Dosimetry," Presented at 9th Intern. Conf. Solid State Detectors, Neuherberg/Munich, 30 Sept.-6 Oct., 1976.
16. D. Hankins, *A Small, Inexpensive Albedo-Neutron Dosimeter*, Los Alamos Scientific Laboratory, Rept. LA-5261 (1973).
17. M. J. Berger and S. M. Seltzer, *Nucl. Instr. Meth.* **104**, 317 (1972).
18. *Hazards Control Progress Report No. 47*, Lawrence Livermore Laboratory, Rept. UCRL-50007-73-3 (1974), p. 14.
19. *Hazards Control Progress Report No. 48*, Lawrence Livermore Laboratory, Rept. UCRL-50007-74-1 (1974), p. 20.
20. *Hazards Control Progress Report No. 50*, Lawrence Livermore Laboratory, Rept. UCRL-50007-75-1 (1975), p. 10.
21. *Hazards Control Progress Report No. 44*, Lawrence Livermore Laboratory, Rept. UCRL-50007-72-3 (1972), p. 3.
22. *Hazards Control Progress Report No. 47*, Lawrence Livermore Laboratory, Rept. UCRL-50007-73-3 (1973), p. 19.
23. W. L. Pickles and J. L. Cate, "Quantitative Non-dispersive X-Ray Fluorescence Analysis of Highly Radioactive Samples of Uranium and Plutonium," in *Advances in X-Ray Analysis*, Vol. 17 (Plenum Press, New York, 1973).
24. J. L. Cate and G. W. Campbell, *Transmission Anode X-Ray Tubes: An Alternate Source of Monoenergetic X-Rays*, Lawrence Livermore Laboratory, Rept. UCRL-77673 (1974).
25. *Hazards Control Progress Report No. 52*, Lawrence Livermore Laboratory, Rept. UCRL-50007-76-1 (1976), p. 10.
26. *Hazards Control Progress Report No. 52*, Lawrence Livermore Laboratory, Rept. UCRL-50007-76-1 (1976), pp. 26-31.
27. C. R. Allen, "HEPA Filter Waste Studies," *Commercial Alpha Waste Program Quarterly Progress Report, July-September 1974*, Hanford Engineering Development Laboratory, Rept. HEDL TME 74-61 (1974).
28. H. J. Ettinger, J. C. Elder and M. Gonzales, *Performance of Multiple HEPA Filters Against Plutonium Aerosols*, Los Alamos Scientific Laboratory, Prog. Rept. LA-5349-PR (1973).

29. R. W. Wood, K. J. Grossaint and T. L. McFeeters, "Exhaust Filtration on Gloveboxes Used for Aqueous Processing of Plutonium," 14th ERDA Air Cleaning Conference, Sun Valley, Idaho, 1976.
30. Thermo-System, Inc., St. Paul, Minn.
31. B. Y. H. Liu, K. T. Whitby and H. H. S. Uy, *Rev. Sci. Instr.* 38, 100 (1967).
32. T. T. Mercer, *Health Phys.* 10, 873 (1964).
33. R. D. Rivers, *A.S.H.R.A.E. Journal* (Feb. 1962), p. 37.
34. G. Zebel, *J. Colloidoil Sci.* 20 522 (1965).
35. G. O. Nelson, W. Bergman, R. D. Taylor, H. H. Miller, A. H. Biermann and C. P. Richards, *Enhanced Filtration Progress Report, July-September 1976*, Lawrence Livermore Laboratory, Rept. UCID-16949-76-3 (1976).
36. *COOLC and FERDOR, Spectra Unfolding Codes*, Oak Ridge National Laboratory, RSIC Computer Code Collection, PSR-17 (1974).
37. *FORIST, Neutron Spectrum Unfolding Code*, Oak Ridge National Laboratory, RSIC Computer Code Collection, PSR-92 (1976).
38. R. H. Johnson, B. W. Wehring, and J. J. Dorning, *Trans. Am. Nucl. Soc.* 22, 798 (1975).
39. R. H. Johnson, *A User's Manual for COOLC and FORIST*, Purdue University, Rept. PNE-75-107 (1975).